



25

Abstract

26 Mesoscale bands develop within winter cyclones as concentrated regions of locally enhanced
27 radar reflectivity, often producing intensified precipitation rates lasting several hours. Surface
28 precipitation characteristics are governed by the microphysical properties of the ice-phase
29 particles aloft, yet their unique microphysical evolutionary pathways and ambient environmental
30 dependencies in banded regions remain poorly understood, in part due to a paucity of
31 observations within natural clouds. Addressing this need, the Investigation of Microphysics and
32 Precipitation for Atlantic Coast-Threatening Snowstorms recently measured properties of winter
33 cyclones from airborne in situ and remote sensing platforms. Observations collected within a
34 banded region of a decaying-stage northeast United States cyclone revealed a microphysical
35 pathway characterized by precipitation fallout from a weak generating cell layer through an ~2
36 km deep subsaturated downdraft region. Sublimation was a dominant evolutionary process,
37 resulting in > 70% reduction of the initial ice water content (IWC). This vertical evolution was
38 reproduced by a 1D particle-based model simulation constrained by observations, conveying
39 accuracy in the process representation. Four sensitivity simulations assessed evolutionary
40 dependencies based on observationally-informed perturbations of the ambient relative humidity,
41 RH, and vertical air motion, w . Perturbations of ~2% RH significantly varied the resultant IWC
42 loss, as much as 29%, whereas comparable perturbations of w had negligible effects. Intrinsic
43 particle evolution during sublimation demonstrated a notable imprint on vertical profiles of radar
44 reflectivity, but Doppler velocity was more strongly governed by the ambient w profile. These
45 findings contextualize radar-based discrimination of sublimation from other ice-phase processes,
46 including riming and aggregation.



47 **1. Introduction**

48 The microphysical pathways for precipitation evolution within winter storms are uniquely
49 dependent on physical properties of the storm across synoptic to microscales that vary
50 temporally and spatially. Consequently, winter storms exhibit significant heterogeneities in
51 precipitation intensity and distribution. Northeast U.S. winter cyclones commonly develop
52 mesoscale banded regions which can produce intense rain- and snowfall rates within
53 concentrated regions of the storm (Novak et al., 2004, 2008; Ganetis et al., 2018). These
54 mesoscale bands are readily diagnosed from composite radar reflectivity measurements such as
55 the operational NWS Multi-Radar Multi-Sensor product (MRMS; Zhang et al., 2011; Brodzik,
56 2022b). Novak et al. (2006) defined a mesoscale band as having a length > 250 km, width of 20
57 to 100 km, and radar reflectivity > 30 dBZ for at least 2 h. Precipitation rates within these
58 potentially high-impact mesoscale bands are challenging to predict, in part because of the
59 demonstrated variations in microphysical properties and evolutionary processes, including rapid
60 changes in crystal habits (Stark et al., 2013) and degrees of riming (Colle et al., 2014) measured
61 at the surface.

62 Mesoscale banding developed during a significant midlatitude cyclone on 4 February 2022
63 that produced widespread and diverse wintry-mixed precipitation spanning the midwest to
64 northeast U.S. At the surface, the cyclone was defined by a relatively weak, elongated low-
65 pressure center and stationary frontal boundary positioned along the U.S. northeastern coastline
66 (Zaremeba et al., 2024). As described in DeLaFrance et al. (2024b, see Fig. 2a and sec. 2.1), two
67 distinct regions of enhanced composite reflectivity developed northeast of the low-pressure
68 center. One of the regions of enhanced reflectivity was positioned on the warm side of the frontal
69 boundary and lacked well-defined banding structure but produced transitory mixed-phase wintry



70 precipitation including rain, ice pellets, and snow over the southern New England region. A
71 second region developed near the surface stationary front that extended into New Hampshire and
72 Maine and exhibited a well-defined banded structure, but with decreasing composite reflectivity
73 in time. Nonetheless, the reflectivity in this banded region was consistently 6.5 to 9.0 dB greater
74 than in the region that lacked well-defined banding. This relative and persistent enhancement in
75 reflectivity in the banded region despite its apparent decay in time raises interesting questions
76 about the evolutionary pathways for precipitating particles in this region and their implications
77 for surface precipitation.

78 Radar reflectivity measurements have a long history of use in estimating precipitation rates,
79 initially from simple empirically derived relationships between reflectivity and rain rate (e.g.,
80 Marshall and Palmer, 1948) and later extended to snowfall rates (e.g., Boucher and Wieler, 1985;
81 Fujiyoshi et al., 1990; Heymsfield et al., 2016). Ambiguity in precipitation intensity due to
82 varied microphysical particle properties has motivated the adoption of more complex
83 relationships derived from an improved understanding of the unique effects of microphysical
84 processes-based evolution on radar remote sensing measurements. Often these techniques are
85 derived from two or more coincident radar-based measurements (e.g., Grecu et al., 2016; Chase
86 et al., 2022; Dunnavan et al., 2023). Leveraging scattering dependencies based on the physical
87 properties of ice crystals and calculations based on modeled snowflakes of varied complexities
88 have shown promise in characterizing the unique effects of ice-phase microphysical processes
89 from coincident radar-based sources (e.g., Petty and Huang, 2010; Kneifel et al., 2011, 2015;
90 Leinonen and Moisseev, 2015; Leinonen and Szyrmer, 2015). Similarly, leveraging
91 dependencies of intrinsic particle fall velocity on their physical properties (e.g., Mitchell, 1996;
92 Heymsfield and Westbrook, 2010) and incorporating measurements from the radar Doppler



93 spectrum provides further constraint on process-based changes, especially during riming (e.g.,
94 Kalesse et al., 2016; Mason et al., 2018, 2019). Through development of novel methods to detect
95 and quantify the effects of microphysical processes from remote sensing radar measurements,
96 physical properties of the natural particles may be more accurately estimated. However, as these
97 retrieval techniques continue to become increasingly complex and adopt multi-source
98 measurements, validation of retrieved physical properties and inferred microphysical processes
99 using observations from natural clouds remains crucially important.

100 Addressing this observational need, the Investigation of Microphysics and Precipitation for
101 Atlantic Coast-Threatening Snowstorms (IMPACTS) field campaign collected measurements
102 from natural precipitating clouds over the northeast and midwest U.S. during 36 science flights
103 over the 2020, 2022, and 2023 winters using a comprehensive suite of remote sensing and in situ
104 instruments (McMurdie et al., 2022a). Eleven science flights were conducted during the 2022
105 deployment with eight of those including coordination between the in situ cloud-sampling P-3
106 and overflying ER-2 aircraft providing coincident remote sensing and in situ measurements
107 within diverse winter storm environments (McMurdie et al., 2022b). These measurements have
108 direct application towards validating remote sensing retrieval of microphysical properties of ice
109 crystals (e.g., Chase et al., 2020, 2022; Matrosov et al., 2022; Finlon et al., 2022; Heymsfield et
110 al., 2023).

111 Elucidating process-based insights from temporally and spatially discontinuous airborne
112 measurements within an evolving and moving cloud system remains challenging. Numerical
113 modeling simulations are one method of connecting independent observations to microphysical
114 processes. However, bulk schemes require a limited representation of particle properties and
115 microphysical processes, thus presenting challenges for the integration of, or comparison with,



116 observations (Morrison et al., 2020). Moreover, three-dimensional dynamic simulations of winter
117 storms are subject to extrinsic uncertainties from design choices including initial conditions,
118 grid-cell resolution, and lead time (e.g., Colle et al., 2023). However, recent advances in
119 Lagrangian particle-based modeling techniques have shown promise in accurately simulating
120 ice-phase precipitation processes, typically at the expense of simplified dynamics and physical
121 domains (e.g., Jensen and Harrington, 2015; Brdar and Seifert, 2018; Bringi et al., 2020;
122 DeLaFrance et al., 2024a).

123 Recently, DeLaFrance et al. (2024b) used one-dimensional particle-based modeling
124 simulations constrained by IMPACTS observations to elucidate process-based insights on the
125 evolution of precipitating particles within the region of the 4 February 2022 winter storm that
126 lacked well-defined banding. Within this region of concurrent vapor deposition, efficient
127 aggregation, and riming, simulated particle evolution revealed that rime accumulations
128 accounted for a dominant 55% of the total ice-phase precipitation mass. Additionally, the riming
129 process produced a unique change in the vertical profile of Doppler velocity, consistent with the
130 coincident remote sensing radar observations. For this riming-dominant evolutionary pathway,
131 sensitivity simulations designed from observationally-informed perturbations of ambient
132 supercooled liquid water concentrations yielded a precipitation rate variability exceeding 60%
133 (DeLaFrance et al., 2024b). These perturbed states further demonstrated substantial variations in
134 reflectivity and Doppler velocity that emphasized differential effects of riming and aggregation
135 processes. These results warrant further investigation on the implications for the dependencies of
136 other ice-phase microphysical processes on their ambient environmental properties; in particular,
137 those associated with the banded region during this same event. With this motivation, this paper
138 aims to address four specific questions,



139

- 140 1. What was the microphysical evolutionary pathway of precipitating particles that
141 contributed to enhanced reflectivity along a mesoscale band during this IMPACTS winter
142 storm event?
- 143 2. What is the role of the ambient environment of the evolving particles in governing
144 precipitation fallout within the banded region?
- 145 3. What are the quantitative implications of sensitivities in the evolution of ice-phase
146 particles to their ambient environment properties?
- 147 4. To what extent are radar remote sensing measurements of reflectivity and Doppler
148 velocity modulated by process-based responses to perturbations in ambient
149 environmental properties?

150

151 To address these questions, we use numerical modeling simulations constrained by
152 IMPACTS observations from the banded region to assess process-based sensitivities and
153 quantify their imprint on radar remote sensing measurements. In the following section, we
154 introduce the IMPACTS instrumentation and observational strategy during the 4 February 2022
155 winter storm. Section 3 provides an observational analysis of the precipitation processes during
156 this event. In Section 4, we establish a control simulation and discuss its observational
157 validation. Section 5 describes four sensitivity simulations to assessing process-based
158 dependencies on the ambient environment. We provide some context for, and discuss the utility
159 of, our findings in Section 6 and offer concluding remarks in Section 7.

160

161



162 **2. Observations from a banded region of enhanced reflectivity during IMPACTS**

163 **2.1. The 4 February 2022 winter storm**

164 Because of the objective of IMPACTS to sample banded precipitation and that the colder
165 region to the north and west of the surface front presented a greater likelihood of snowfall at the
166 surface, the banded region near the front was the primary target of the 4 February science flights.
167 With passage of this band, diverse winter precipitation characteristics were reported at
168 Automated Surface Observing Stations (ASOS; Brodzik, 2022a) in Maine. Between 00:00 UTC
169 4 and 00:00 UTC 5 February, Portland, ME (KPWM; Fig. 1a) reported a mixture of rain,
170 freezing rain, snow, and ice pellets while Bangor, ME (KBGR; Fig. 1a) experienced a transition
171 from rain to snow by 01:25 UTC, which persisted through the duration of the storm. The
172 Wiscasset, ME (KIWI; Fig. 1a) station reported a similar diversity in precipitation type as
173 KPWM, with a modest peak hourly precipitation rate of 2.5 mm during the 12:00 UTC hour and
174 a gradual reduction in intensity thereafter.

175 IMPACTS executed a semi-Lagrangian aircraft sampling strategy consisting of six flight legs
176 in a “lawnmower-style” arrangement oriented orthogonal to the band from approximately 14:00
177 to 18:00 UTC (Fig. 1). In contrast to sampling an evolving and moving storm along a flight leg
178 fixed in space at varied altitudes (i.e., Eulerian), an advantage of Lagrangian sampling is that it
179 attempts to maintain temporal and spatial continuity of the storm and the precipitating particles
180 therein. Towards the objective of Lagrangian sampling, the P-3 aircraft, equipped with in situ
181 cloud probes, flew at a high altitude initially and descended with each subsequent constant
182 altitude leg, while horizontally translating with the storm. The ER-2 was equipped with remote
183 sensing instrumentation and flew in coordination with the P-3 above the storm at constant
184 altitude of approximately 20 km a.m.s.l. To minimize temporal differences between the two

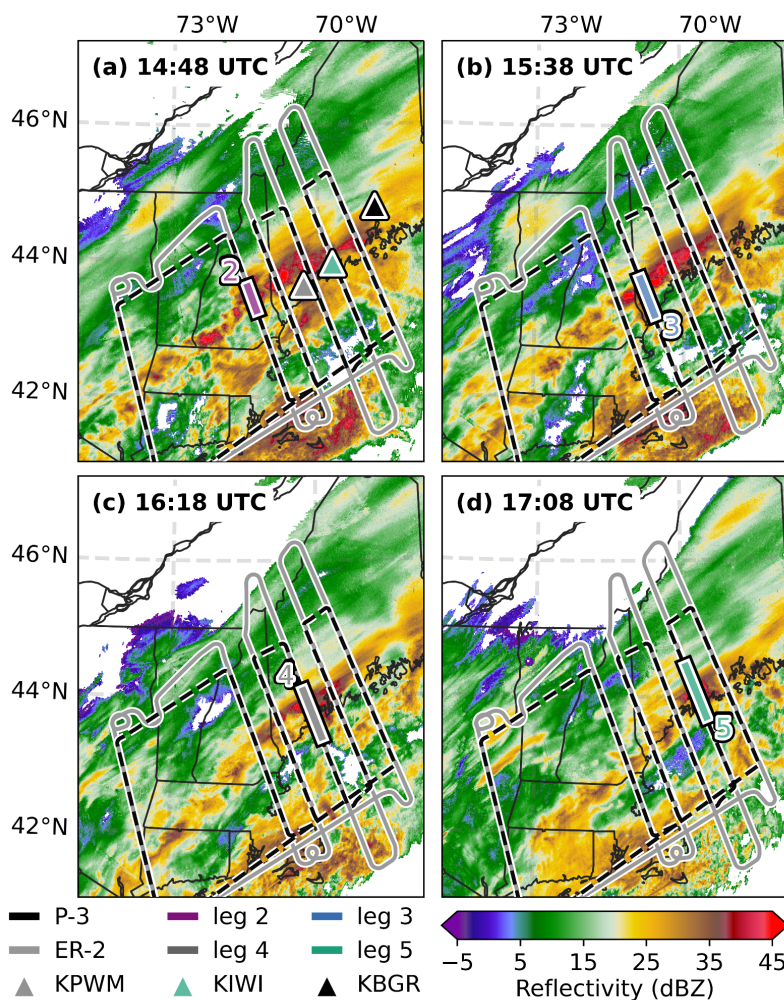


185 aircraft owing to their differential air speeds, each aircraft sampled the center points of the flight
186 legs at nearly the same time and the center points were positioned near the band's reflectivity
187 maxima.

188 On the initial flight leg, the P-3 sampled at a constant altitude of 6.2 km a.m.s.l. intersecting
189 the far western edge of the band. Flight leg 2, at an altitude of 5.5 km a.m.s.l., was positioned
190 northeast to better intersect the region of enhanced radar echo. The remaining legs were
191 positioned northeast of the previous leg at a distance that approximated the storm's advective
192 speed, each at a lower altitude and intersected the melting level on the final flight leg at 3.0 km
193 a.m.s.l. This Lagrangian strategy requires that the storm maintain steady state during sampling.
194 Thus, we suggest that flight legs 2 through 6 provided semi-Lagrangian context for coincident in
195 situ and remote sensing measurements of the cloud and precipitation particles during evolution
196 between 5.5 and 3.0 km a.m.s.l. To constrain our analysis to the ice-phase precipitation processes
197 within this storm, in situ and remote sensing measurements from flight legs 2 through 5 (5.5 to
198 3.6 km a.m.s.l.) are used. Measurements collected between sampling along flight leg 2 (~14:45
199 UTC, Fig. 1a) and flight leg 5 (~17:15 UTC, Fig. 1d) occurred as the maximum composite
200 reflectivity within the banded region weakened from 54.5 to 47.5 dBZ, suggesting a decay of
201 storm intensity, consistent with the reduction in precipitation rates during the same time period.

202

203



204

205 **Figure 1:** Flight tracks for the ER-2 and P-3 on 4 February 2022 and composite reflectivity
206 from the NWS MRMS product at the time of aircraft sampling within the region of analysis at
207 each flight leg as indicated by the colored lines. ASOS surface locations for Portland, ME
208 (KPWM), Wiscasset, ME (KIWI), and Bangor, ME (KBGR) are shown in panel (a).
209

210 2.2. IMPACTS observational assets

211 The IMPACTS campaign benefited from a comprehensive suite of aircraft-based in situ and
212 remote sensing instrumentation onboard the cloud-penetrating P-3 and overflying ER-2 aircrafts.
213 From these instruments, the in situ measurements of precipitating particle properties and their



214 ambient environmental conditions coincident with remote sensing radar are crucial towards
215 addressing our research questions.

216 The P-3 aircraft was equipped with several particle probes to derive quantitative measures of
217 the physical properties and concentrations of ice- and liquid-phase populations of particles.
218 Measurements of the ice-phase particle size distributions (PSD) were derived from a vertically
219 oriented High-Volume Precipitation Spectrometer (HVPS) probe (Bansemer et al., 2022). The
220 HVPS is an Optical Array Probe (OAP), which permits sizing of a sampled ice crystal based on a
221 two-dimensional projected image (Lawson et al., 1993) from a 128-element array with a pixel
222 resolution of 150 μm (Bansemer et al., 2022). Thus, the HVPS is ideally suited to measuring
223 larger ice crystals, ~ 0.5 to 30.0 mm diameter. Commonly, the HVPS is paired with a Two-
224 Dimensional-Stereo (2D-S) OAP which also has a 128-element array but at a higher resolution of
225 10 μm and, therefore, is ideally suited for measuring small ice crystals. However, because the
226 2D-S did not operate during the 4 February flight, our analysis uses HVPS measurements to
227 derive in situ PSDs from ice crystals of diameters, D , > 0.5 mm. Measurements of the liquid-
228 phase particle population were derived from the Fast Cloud Droplet Probe (FCDP), a component
229 of the HAWKEYE combination probe, to estimate droplet sizes within a range of 2 to 50 μm
230 based on principles of Mie light scattering (Lawson et al., 2017). The National Center for
231 Atmospheric Research (NCAR) provided processing of the 1 Hz particle probe data (Bansemer
232 et al., 2022).

233 Particle imagery provides crucial evidence of the unique habits and geometric properties of
234 the ice crystals and permits inferences of the microphysical processes by which they evolved.
235 We use imagery collected from the Particle Habit Imaging and Polar Scattering Probe (PHIPS); a
236 novel instrument composed of two cameras separated by 120° with a resolution of 2 μm within a



237 field of view of approximately 3 x 2 mm (Schnaiter, 2022). For ambient environmental context,
238 in situ meteorological properties were measured by instrumentation onboard the P-3 aircraft to
239 derive pressure, temperature, dew point, and water vapor (Yang-Martin and Bennett, 2022).
240 Measurements of the three-dimensional ambient wind field were obtained from the Turbulent Air
241 Motion Measurement System (TAMMS; Thornhill, 2022). The TAMMS instrument is a system
242 of sensors distributed across the aircraft to estimate the horizontal and vertical components of the
243 winds and for configuration on the P-3 aircraft yields an estimated accuracy of 0.2 m s^{-1} for the
244 horizontal and vertical wind speeds (Thornhill et al., 2003; Thornhill, 2022). Supplementing the
245 IMPACTS airborne measurements, ambient meteorological conditions were obtained from
246 operational rawinsondes at NWS launch sites (Waldstreicher and Brodzik, 2022). Additionally,
247 standard NWS operational measurements including ASOS station data and composite radar from
248 the MRMS product were used to assess the surface conditions and provide large-scale context
249 during IMPACTS events.

250

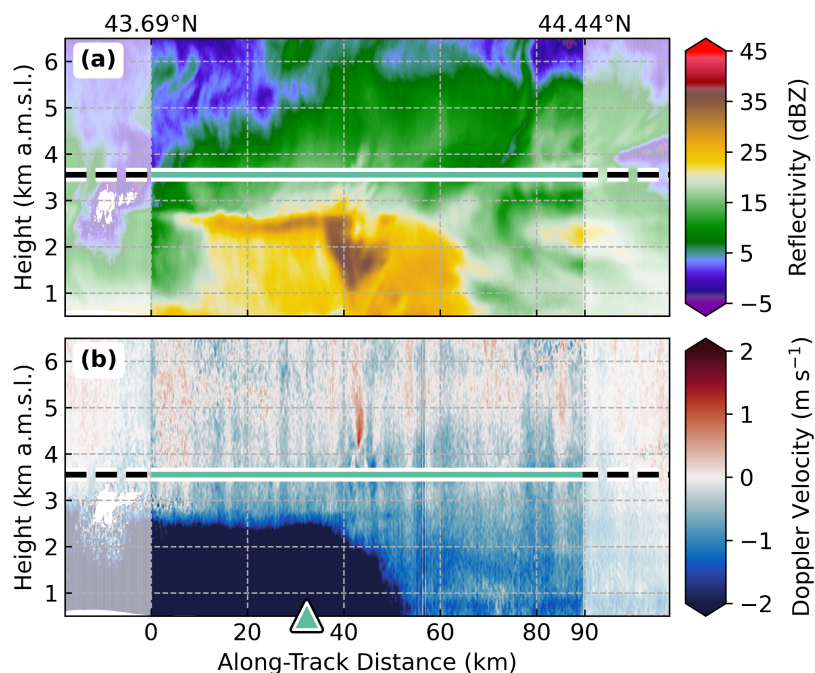
251

252

253

254

255



256

257 **Figure 2:** Vertical cross sections of HIWRAP Ku-band radar (a) reflectivity and (b) Doppler
258 velocity from the ER-2 flight leg 5 as shown in Fig. 1d. Coincident sampling from the P-3
259 aircraft occurred at 3.6 km a.m.s.l. and the in situ observational extent assessed by frontal
260 analysis is indicated by the horizontal green line. The marker in panel (b) locates the KIWI
261 (Wiscasset, ME) ASOS surface station positioned ~2.5 km west of the flight leg (see Fig. 1a).
262

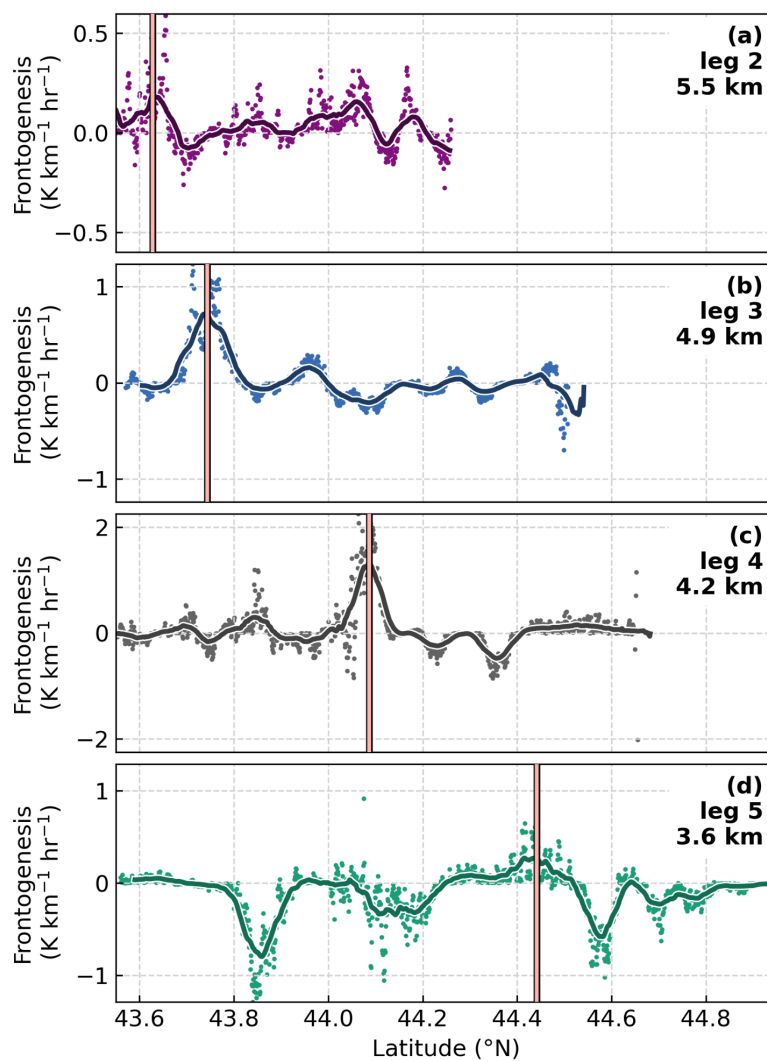
263 The 4 February event was sampled by radar from the high-altitude ER-2 aircraft at Ku (13.9
264 Ghz), Ka (35.6 Ghz), and W bands (94 GHz). For radar reflectivity and Doppler velocity, we use
265 measurements collected from the dual-band (Ku and Ka) High-Altitude Wind and Rain Airborne
266 Profiler (HIWRAP; McLinden et al., 2022), which has a vertical resolution of 150 m (Li et al.,
267 2016). As an example of one flight leg, Fig. 2 shows the vertical cross section of Ku-band
268 reflectivity, Z_{Ku} , and Doppler velocity, $V_{D_{Ku}}$, from the HIWRAP radar onboard the ER-2 as it
269 overflew the frontal band on flight leg 5 between ~17:08 and ~17:16 UTC. The P-3 aircraft
270 sampled this location at 3.6 km a.m.s.l. between ~17:05 and ~17:17 UTC. At the center point
271 over the band, the time difference between the two aircraft was 91 seconds. During flight leg 5,



272 the two aircraft overflow the KIWI ASOS station, which reported a precipitation rate of 1.02 mm
273 h^{-1} at its location ~ 2.5 km west of the flight leg (Fig. 1a) and on the warm side of the frontal
274 boundary. At KIWI, a radar bright band signature of the melting level occurs near 3 km a.m.s.l.
275 The northward extent of the surface front is marked by the abrupt termination of the melting
276 level to the surface near 50 km along-track distance which is most apparent in the V_{D_Ku} gradient
277 (Fig. 2b) associated with the change in fall velocity of melting ice-phase particles.

278 The banded region was associated with a prominent cloud aloft, extending to about 6 km
279 a.m.s.l. Substantial decreases in Z_{Ku} were apparent immediately above a distinct vertical gradient
280 in Z_{Ku} at 6 km a.m.s.l. (Fig. 2a). This vertical Z_{Ku} gradient exhibited small-scale [$O(1$ km)]
281 structural variabilities and filaments in Z_{Ku} down to the melting level. Similar small-scale [$O(1$
282 km)] structural variabilities were present in V_{D_Ku} near 6 km a.m.s.l., and within a background of
283 negative V_{D_Ku} , there were several isolated regions of substantial updrafts. Below 5 km a.m.s.l.,
284 V_{D_Ku} became increasingly negative, which indicated either increasing particle fall velocities or a
285 reduction in, or reversal of, ambient updrafts. The vertical cloud structure sampled by the ER-2
286 radar on flight leg 5 is suggestive of a weak generating cell layer near 6 km. a.m.s.l. and
287 precipitation fallstreaks (e.g., Rosenow et al., 2014; Plummer et al., 2014) towards the banded
288 region below.

289



290

291 **Figure 3:** Frontogenesis computed from 1 Hz in situ measurements (dots) with smoothing
292 using a 60-s rolling mean (horizontal line) to estimate a maximum (vertical lines) along
293 individual P-3 flight legs 2 to 5. Mean altitudes of the P-3 are stated for each flight leg.
294

295

296

297



298 **2.3. Observational context of in situ measurements**

299 At either edge of the banded region, the horizontal extent of cloud aloft is marked by distinct
300 gradients in Z_{Ku} (Fig. 2a). At the northern edge, a reduction in Z_{Ku} occurs at a region of
301 significant shear in the precipitation fallstreaks, which is expected with a wind shift along a
302 frontal boundary. Therefore, we use the in situ environmental measurements to objectively
303 identify the location of the frontal boundary, establishing flight-leg specific observational
304 domains (i.e., observational regions indicated in Fig. 1) that preserve the intended Lagrangian in
305 situ sampling of the evolving ice-phase particles.

306 The northern extent of the horizontal observational domain is identified by a frontogenesis
307 maximum. We compute frontogenesis from P-3 in situ measurements of horizontal winds, u and
308 v , and potential temperature, θ , using the two-dimensional form of the (Miller, 1948) equation,

309
$$F_{2D} = \frac{1}{|\nabla\theta|} \left[-\frac{\partial\theta}{\partial x} \left(\frac{\partial u}{\partial x} \frac{\partial\theta}{\partial x} + \frac{\partial v}{\partial x} \frac{\partial\theta}{\partial y} \right) - \frac{\partial\theta}{\partial y} \left(\frac{\partial u}{\partial y} \frac{\partial\theta}{\partial x} + \frac{\partial v}{\partial y} \frac{\partial\theta}{\partial y} \right) \right].$$

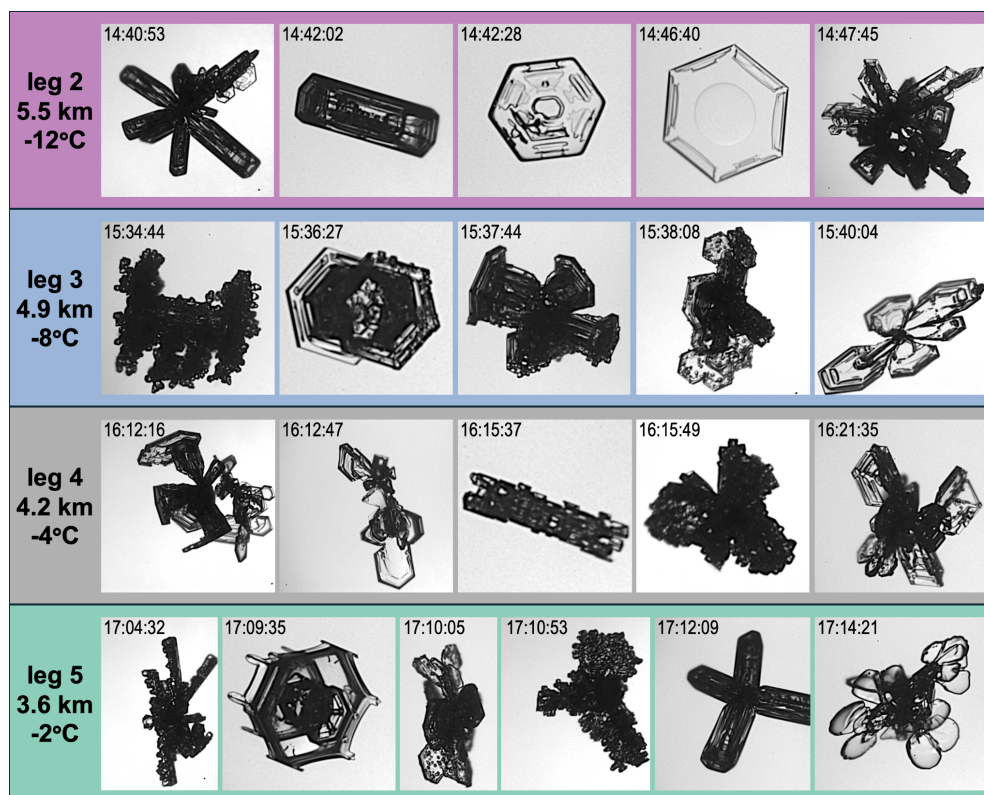
310

311 Because of the considerable noise in frontogenesis computed from the 1Hz measurements,
312 we apply a smoothing using a 60-s rolling mean (Fig. 3). We assess the northern extent of the
313 observational domain for each flight leg by identifying a relative maximum in the smoothed
314 frontogenesis. The frontogenesis analysis indicates a frontal boundary with an apparent
315 northward gradient with increasing height, which primarily results from the southwest-to-
316 northeast orientation of the band. In addition, a northward sloping frontal boundary formed from
317 the warmer air mass to the south overrunning the cold surface air mass to the north.

318 At the southern edge of the band, there was a distinct absence of cloud during most of the
319 aircraft sampling along flight legs 2 through 5 (Fig. 1a-d). Thus, we assess the southern edges of
320 the observational domain at the altitude of the P-3 as the cloud edge. At each flight leg, we use



321 Z_{Ku} measurements at height of the P-3 aircraft to identify a reduction in Z_{Ku} below 0 dBZ. An
322 exception is made for flight leg 3, which intersected a transient cloud (Fig. 1b), where we instead
323 identify a relative minimum in Z_{Ku} (~ 5 dBZ). All further in situ observations used for analysis in
324 this study were obtained from within these flight-leg specific cloud-edge-assessed southern
325 points and the frontal-boundary-assessed northern points (Fig. 1). Constrained by this approach,
326 the evolutionary pathway of particles reaching the surface is identified by observations of the
327 particle properties and their ambient environment collected within the cloud aloft at four
328 altitudes descending in time.



329

330 **Figure 4:** Particle imagery collected from the PHIPS probe within the banded regions of P-3
331 flight legs 2 to 5. Images are intended for representation of the crystal properties only and are not
332 to scale. Mean altitudes of the P-3 and ambient temperatures are stated for each flight leg.
333



334 Particle imagery collected from the PHIPS probe on P-3 flight legs 2 through 5 are shown in
335 Fig. 4. At 5.5 km a.m.s.l. and an ambient air temperature of -12°C , a remarkable diversity of
336 crystal habits was observed including single crystal columns (e.g., 14:42:02 UTC), plates (e.g.,
337 14:42:28 and 14:46:40 UTC), and dendrites as well as polycrystalline structures of plates,
338 dendrites, and sideplanes (e.g., 14:47:45 UTC) and bullet rosettes (e.g., 14:40:53 UTC). Some of
339 the particles at 5.5 km a.m.s.l. showed evidence of sublimation (e.g., 14:42:28 UTC) in the form
340 of rounded corners and a smooth, glossy appearance (Nelson, 1998). With descent on subsequent
341 flight legs, there was increasing evidence of sublimation. However, beginning at flight leg 3 at
342 4.9 km a.m.s.l. where the ambient temperature was -8°C and relative humidity (RH), 83%, there
343 was also evidence of riming with varied degrees of accumulated supercooled liquid water
344 droplets (e.g., 15:34:44 and 15:36:27 UTC). Similarly diverse crystal habits with varied degrees
345 of rime accumulation and sublimation were observed in imagery collected on flight leg 4 (4.2 km
346 a.m.s.l., -4°C , 82% RH) and flight leg 5 (3.6 km a.m.s.l., -2°C , 80% RH).

347 From imagery collected at all heights, relative to the prevalence of single crystals, very few
348 aggregate particles were observed. This near absence of aggregation significantly contrasts with
349 the high prevalence of aggregate particles observed within the southern region of enhanced
350 reflectivity that lacked well-defined banding (DeLaFrance et al., 2024b). However, riming was
351 evident in both regions. The presence of riming among particle populations at flight legs 3
352 through 5 suggests a mixed-phase layer with an upper boundary between 4.9 and 5.5 km a.m.s.l.,
353 but riming occurred heterogeneously throughout the mixed-phase layer. Interestingly,
354 populations of rimed particles were observed in close proximity to sublimated particles (e.g.,
355 15:38:08 and 15:40:04 UTC). Additionally, some particles appear to have experienced riming
356 followed by sublimation at some later time (e.g., 17:10:05 UTC), whereas others appear to only



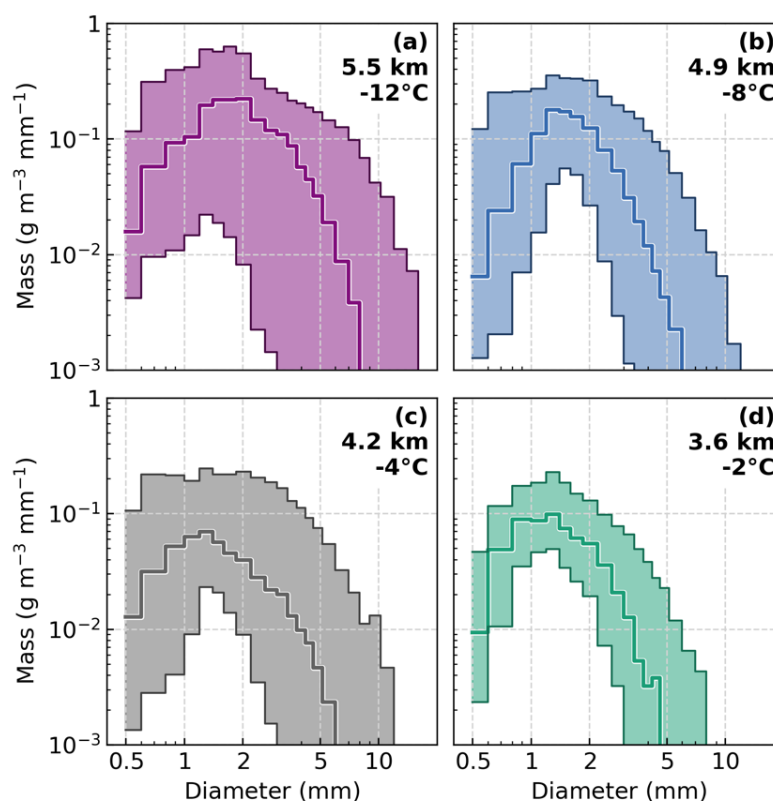
357 experienced sublimation between formation aloft and 3.6 km a.m.s.l. (e.g., 17:12:09 UTC).
358 Collectively, particle imagery from above the band indicates a dominant microphysical process
359 between 5.5 and 3.6 km a.m.s.l. was sublimation. In Section 3, we use in situ measurements to
360 quantify the evolutionary effects of these observed microphysical processes on the ice-phase
361 particles and provide environmental context through assessment of the ambient cloud properties.
362

363 **3. Properties of evolving ice-phase particles and their ambient environment**

364 Precipitation rates at the surface are governed by the particle mass and its rate of fallout from
365 cloud above. To determine the surface implications, we first quantify the initial ice-phase
366 precipitation mass aloft, at 5.5 km a.m.s.l., and its evolution within cloud between 5.5 and 3.6
367 km a.m.s.l. Figure 5 shows the median and interquartile range (IQR, 25th and 75th percentile) ice
368 mass PSDs from HVPS measurements of particles with $D > 0.5$ mm from P-3 flight legs 2
369 through 5. Consistent with DeLaFrance et al. (2024b), we assume a mass–dimension relationship
370 following Brown and Francis (1995). The greatest ice mass concentration and largest particle
371 sizes were identified at 5.5 km a.m.s.l. Additionally, we found the most variability expressed by
372 the IQR of PSDs at this height. However, based on the observed diversity among crystal habits at
373 5.5 km a.m.s.l. (Fig. 4), this variability in the observed PSD is not surprising. Although
374 measurements of ice at small particle sizes are unavailable for the 4 February event, particles
375 larger than ~ 0.5 mm overwhelmingly dominate the contribution to the total ice water content
376 (IWC) and, thus, the HVPS measurements provide a valid estimate of the precipitation mass. The
377 median IWC at 5.5 km a.m.s.l. was 0.540 g m^{-3} and decreased to 0.278 g m^{-3} at 4.9 km a.m.s.l.,
378 then further decreased to 0.127 g m^{-3} at 4.2 km a.m.s.l. At 3.6 km a.m.s.l., IWC slightly



379 increased to 0.148 g m^{-3} ; however, there was a notable reduction of ice mass at the largest
380 particle sizes, especially relative to 5.5 km a.m.s.l. (Fig. 5a, d).
381



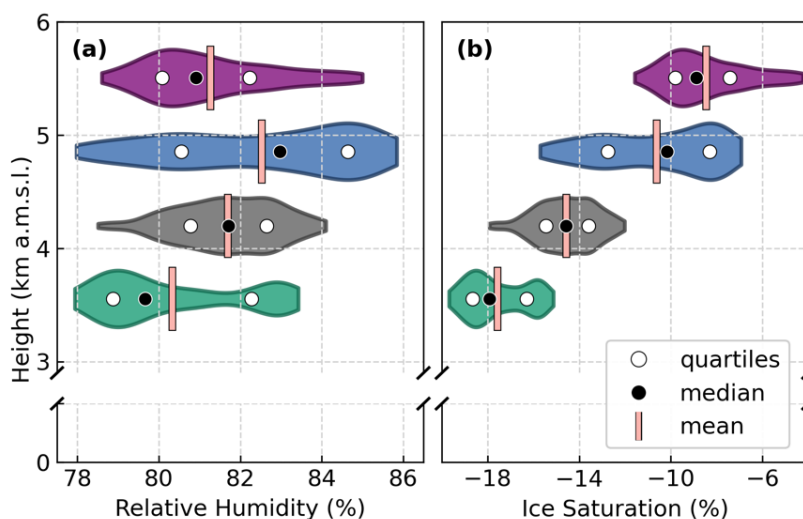
382

383 **Figure 5:** Ice mass PSD median (line) and interquartile range (shaded) in situ measurements
384 from the HVPS probe at particle diameters $> 0.5 \text{ mm}$ within the banded regions of individual P-3
385 flight legs 2 to 5. Mean altitudes of the P-3 and ambient temperatures are stated for each flight
386 leg.
387

388 The relative maximum in ice mass at 5.5 km a.m.s.l. is consistent with the notion of ice-
389 phase particles concentrating aloft along the frontal boundary and maintained within a weak
390 generating cell layer (Fig. 2). Precipitation fallout within the cloud below shows quantitative
391 evidence of sublimation in the IWC loss with descent, while a reduction in particle size,



392 especially among large particles, is consistent with the minimal evidence of aggregation in the
393 imaged particles (Fig. 4). The small increase in IWC between 4.2 and 3.6 km a.m.s.l. occurs
394 among particles ~ 0.5 to 2 mm in size and is most likely a result of accumulated rime mass,
395 despite the concurrent sublimation. Due to intermittency of the FCDP instrument on 4 February,
396 measurements of the supercooled liquid water droplets population in the banded region are
397 available only for flight leg 5 at 3.6 km a.m.s.l. At this height, there was a mean liquid water
398 content (LWC) of 0.02 g m^{-3} and droplet diameter of $17 \text{ }\mu\text{m}$. However, imagery of supercooled
399 liquid droplets and rimed particles suggest that rime accumulation occurred at least as high as 4.9
400 km a.m.s.l (Fig. 4). The prominence of sublimation effects concurrent with riming presents a
401 distinctive evolutionary pathway for losses and accumulations of ice mass and requires a unique
402 ambient environment supportive of these primary processes.
403



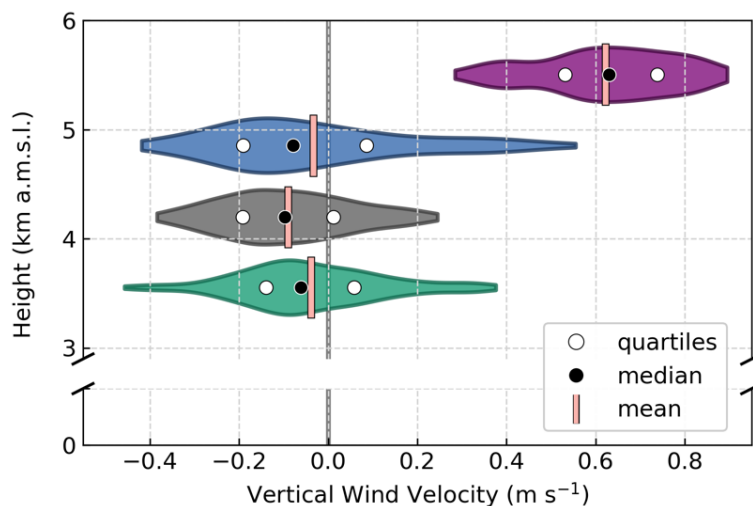
404
405
406
407
408

Figure 6: Violin plot distributions of (a) relative humidity and (b) ice supersaturation in situ measurements within the banded regions of flight legs 2 to 5. Outliers exceeding the 5th and 95th percentiles are not plotted.



409 Subsaturated conditions were found at all heights within the cloud. Figure 6a shows the
410 measured ambient RH with respect to water at each P-3 flight level. The RH was similar through
411 the vertical profile of cloud with median values from 79.7% (3.6 km a.m.s.l.) to 83.0% (4.9 km
412 a.m.s.l.) and the range of variability was typically less than ~5-6% across each flight leg
413 segment. Expressed as saturation with respect to ice in Fig. 6b, the cloud demonstrated an
414 increasingly subsaturated ambient environment with descent. At 5.5. km a.m.s.l. (-12°C), the
415 median ice saturation was -8.9% and further decreased to -17.9% at 3.6 km a.m.s.l. (-2°C). It is
416 not readily apparent whether the magnitude of increasing subsaturation at lower heights (warmer
417 temperatures) is representative of the cloud's natural vertical profile at any given time or a result
418 of the temporal evolution between sampling at flight leg 2 and flight leg 5 (~2 h) within a
419 decaying stage storm. Nonetheless, the subsaturated vertical profile is consistent with the
420 evidence of sublimation among particle images at all heights (Fig. 4). However, riming requires
421 the presence of supercooled liquid water droplets which, although are not sustained in a
422 subsaturated environment, require time to evaporate. For example, within the median observed
423 environmental conditions on flight leg 3 at 4.9 km a.m.s.l. (~83% RH, -8°C), droplets with an
424 initial radius, r_0 , of 10 μm will require ~10 s to evaporate and substantially longer for larger
425 droplets (e.g., ~70 s for $r_0 = 30 \mu\text{m}$; Roy et al., 2023). Supercooled liquid water droplets were
426 likely formed in locally supersaturated environments, which occur within regions of updrafts
427 (e.g., Rauber and Tokay, 1991).

428



429

430 **Figure 7:** Violin plot distributions of in situ measurements of vertical wind velocity from the
431 TAMMS instrument within the banded regions of P-3 flight legs 2 to 5. Outliers exceeding the
432 5th and 95th percentiles are not plotted.
433

434 The distribution of ambient vertical wind velocity, w , measurements from the TAMMS
435 instrument on each P-3 flight leg are shown in Fig. 7. Notably, there was a characteristic ambient
436 updraft at 5.5 km a.m.s.l. and abrupt transition to a weak downdraft below. This w profile is
437 consistent with the notion of a weak generating cell layer with precipitation fallout inferred from
438 the appearance along the prominent cloud top and fallstreaks in Z_{Ku} below ~ 5 km a.m.s.l. from
439 the radar cross section along flight leg 5 (Fig. 2a). At 5.5 km a.m.s.l., the median w was 0.63 m s^{-1} ,
440 which is weaker than updrafts of 1 to 2 m s^{-1} that are common in generating cells within winter
441 cyclones (e.g., Rosenow et al., 2014; Kumjian et al., 2014; Keeler et al., 2016). Between 4.9 and
442 3.6 km a.m.s.l., the ambient median wind field was characterized by weak descent with $w = \sim -$
443 0.06 to $\sim -0.10 \text{ m s}^{-1}$. However, within this cloud layer, variabilities in w were observed, and at
444 all heights, updrafts were identified at the upper quartile of measurements. This range of w
445 variability was similarly evident in horizontal gradients of Doppler velocity across flight leg 5,



446 despite an overall descent below ~ 5 km a.m.s.l. (Fig. 2b). Intermittent updrafts appear to have
447 provided a source of supercooled liquid water within the subsaturated ambient background
448 environment. To support these observational inferences of microphysical processes associated
449 with the band, we use an observationally constrained numerical simulation and quantify the
450 independent process-based effects and their dependencies on properties of the ambient
451 environment for governing the cloud's precipitation mass and rate of fallout.

452

453 **4. Control simulation design and validation**

454 Our modeling environment is designed to permit isolation and direct manipulation of
455 microphysical processes and the ambient environmental conditions to elucidate their independent
456 effects on an evolving ice-phase particle population. Model selection and its design follows
457 DeLaFrance et al. (2024b), which simulated the evolution of precipitating particles associated
458 with the southerly displaced region of enhanced reflectivity on 4 February. As in this prior study,
459 we use the Lagrangian particle-based McSnow model, which has a 1D columnar domain (Brdar
460 and Seifert, 2018). The McSnow model's particle-based scheme evolves an initial population of
461 ice-phase particles through explicit processes of deposition (sublimation), aggregation, and
462 riming within a prescriptive ambient environment. Consistent with the present study's objectives,
463 McSnow permits independent user control of these ice-phase processes, their regions of activity
464 or inactivity within the column, and properties of the ambient environment as prescribed inputs.
465 Furthermore, the ice-phase particle population evolves at the scale of the particle, thereby
466 removing assumptions about the evolving PSD, which is readily accessible throughout the
467 column. For comparability with simulations presented in DeLaFrance et al. (2024b), we maintain



468 consistency in the decisions regarding parameterizations and processing, with select exceptions
469 motivated by observed properties that were unique to each region of the storm.

470 The first step is to create a control simulation that reproduces the observed evolution of
471 precipitating particles within their natural ambient environment using inputs derived from in situ
472 measurements between P-3 flight legs 2 through 5. Particles are introduced in the model such
473 that the initial PSD at the upper boundary remains prescribed, which we derive from a Gamma
474 distribution fitted to the median PSD observed at 5.5 km a.m.s.l. at the uppermost P-3 flight leg
475 (Fig. 5a). This initial PSD is characterized by an estimated IWC of 0.540 g m^{-3} and total number
476 concentration of $7 \times 10^3 \text{ m}^{-3}$ ($D > 0.225 \text{ }\mu\text{m}$). Newly initiated particles have a mass–dimension
477 relationship of $m = 0.00294D^{1.94}$ (cgs) following Brown and Francis (1995) for unrimed crystals
478 but evolve independent of this assumption thereafter. Particle terminal velocity, V_t , is derived
479 following Heymsfield and Westbrook (2010). We specify a column of 500 grid cells, equating to
480 a vertical resolution of 11 m, based on an upper boundary at 5.5 km a.m.s.l. Particles evolve
481 within a prescriptive ambient environment, which is derived from the median value in situ
482 measurements of standard atmospheric properties (i.e., temperature, dew point, RH, pressure) at
483 each flight altitude (Fig. 6), and then linearly interpolating between measurements. Similarly, w
484 is prescribed from linear interpolation between median in situ measurements at each flight
485 altitude (Fig. 7).

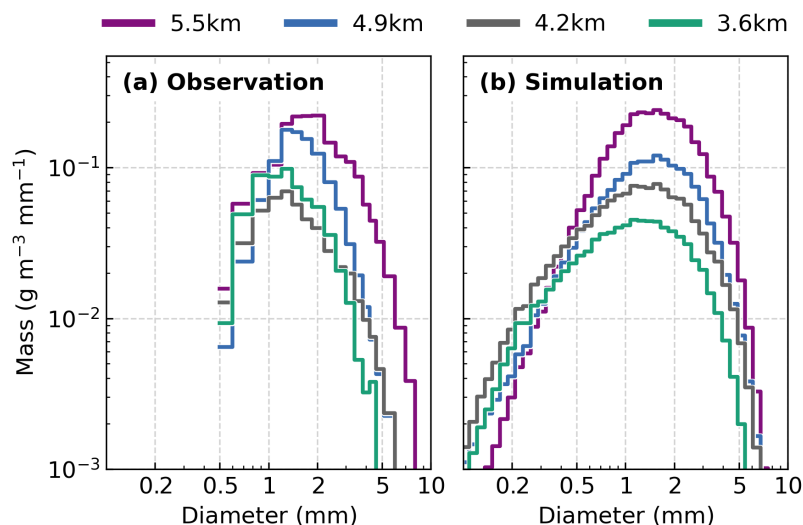
486 The in situ observations of inferred microphysical processes motivated several design
487 considerations. Minimal evidence of aggregation throughout the column among particle imagery
488 (Fig. 4) and an overall reduction in particle sizes with descent in cloud suggest a very low
489 process efficiency. With McSnow, upon collision, two particles will remain joined as an
490 aggregate particle dependent on a sticking efficiency parameter, E_{agg} , which scales from 0 to 1



491 (e.g., Pruppacher and Klett, 1997). Here, we adopt a sticking efficiency based on the laboratory
492 investigations of Connolly et al. (2012) in which they identify a maximum likelihood estimate
493 (MLE) and confidence interval (CI) for a temperature-dependent E_{agg} . Whereas in DeLaFrance et
494 al. (2024b) it was appropriate to adopt an E_{agg} following the upper range of the CI provided in
495 Connolly et al. (2012), here, we find it appropriate to adopt an E_{agg} following the lower range of
496 the CI. Therefore, E_{agg} has a value of 0.4 at -15°C and linearly reduces to 0 at -10°C , which is
497 maintained to 0°C . Because rimed particles were frequently observed in particle imagery at 4.9
498 km a.m.s.l., but not at 5.5 km a.m.s.l. (Fig. 4), we define a mixed-phase layer of cloud below 5.0
499 km a.m.s.l. where riming occurs following a stochastic procedure (Brdar and Seifert, 2018) based
500 on prescriptive properties of the liquid water population. From the FCDP measurements, we
501 specify a LWC of 0.02 g m^{-3} and characteristic droplet radius of $8 \mu\text{m}$. Consistent with
502 DeLaFrance et al. (2024b), all simulations run for 10 h at a time step of 5 s, and average the final
503 5 h, after reaching a steady state, for analysis.

504

505



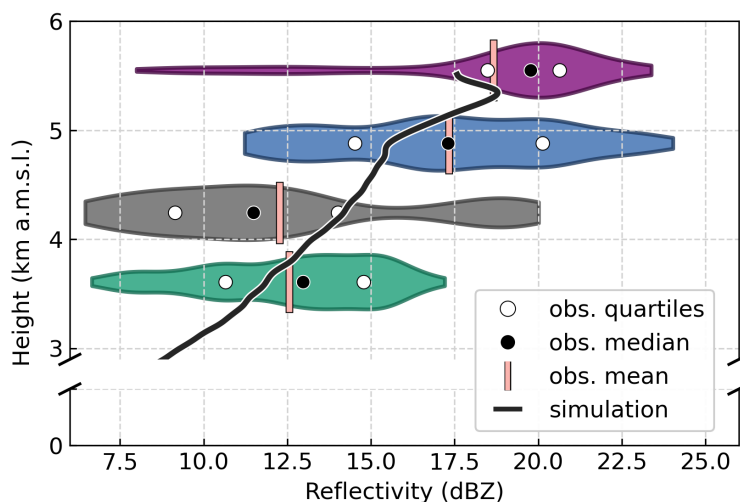
506

507 **Figure 8:** Composite ice mass PSDs from (a) in situ observations within banded regions of
508 P-3 flight legs 2 to 5 (see Fig. 1a-d) and (b) the control model simulation at equivalent heights.
509 Mean altitudes of the P-3 are stated for each flight leg.
510

511 To verify the control simulation, we first assess the evolution of the PSD throughout the ice-
512 phase layer of cloud. Specifically, we compare the model-simulated PSD with the median
513 observed PSD at each P-3 flight altitude. Figure 8a composites the flight-leg specific PSDs at D
514 > 0.5 mm, as shown in Fig. 5. The simulated PSD at equivalent heights from the model are
515 shown in Fig. 8b. A primary criterion towards establishing a successful control simulation was a
516 reproduction of the reduced IWC and particle sizes with descent that was expressed in the
517 observations. The control simulation has a vertical evolution of the PSD that demonstrates
518 consistency with observations, providing confidence that the modeled processes are generally
519 representative of the natural processes. At 5.5 km a.m.s.l., the control simulation has an initial
520 IWC of 0.606 g m^{-3} . Between 4.9, 4.2, and 3.6 km a.m.s.l., IWC decreased to 0.303, 0.214, and
521 0.119 g m^{-3} , respectively. Some of the unique variabilities among the observations are not
522 captured by the simulation. For example, the relative increase in mass at $D = \sim 0.5$ to 2 mm



523 between 4.2 and 3.6 km a.m.s.l. in observations (Fig. 8a) is likely due to accumulation of rime
524 mass. In the control simulation, the rime fraction, the fractional mass attributable to accumulated
525 rime, reaches 0.33 at 3.6 km a.m.s.l., which is consistent with a subjective assessment of rime
526 accumulation among the particle imagery at this height (Fig. 4, leg 5). In the observed cloud,
527 however, supercooled liquid water (and riming) was heterogeneously distributed throughout the
528 mixed-phase layer, which is not represented in the model. While this limitation introduces some
529 uncertainty in the simulated accumulation of rime mass, the relatively small accumulated rime
530 fraction of 0.33 is consistent with our expectations based on prior simulations within the
531 southerly displaced region of enhanced reflectivity (DeLaFrance et al., 2024b). Within that
532 region of the storm, there was an ~500 m deeper mixed-phase layer and higher LWC of 0.05 g
533 m⁻³, compared to 0.02 g m⁻³ within the frontal region, and its similarly-constrained control
534 simulation produced a rime fraction of 0.55.



535

536 **Figure 9:** Ku-band radar reflectivity estimated from the control simulation and violin plot
537 distributions of reflectivity from the ER-2 HIWRAP Ku-band radar at the altitude of the P-3
538 aircraft within the banded regions of P-3 flight legs 2 to 5. Outliers exceeding the 5th and 95th
539 percentiles are not plotted.



540

541 Because we are motivated to identify the imprint of ice-phase microphysical processes and
542 their sensitivities to ambient conditions on radar remote sensing measurements, we further
543 evaluate the control simulation by computing Z_{Ku} from the evolved PSD, which is compared to
544 coincident measurements from the overflying ER-2 HIWRAP. Estimation of radar moments
545 from the simulated PSD follows DeLaFrance et al. (2024b) in applying a T-matrix approach
546 (Leinonen, 2014) to estimate the Ku-band radar backscatter cross section and a two-way path
547 integrated attenuation correction (Williams, 2022). Figure 9 shows the distribution of HIWRAP
548 Z_{Ku} measured at the height of the P-3 aircraft across each flight leg. The observed Z_{Ku} maximized
549 aloft and decreased between 5.5 and 4.2 km a.m.s.l., then slightly increased at 3.6 km a.m.s.l.
550 Throughout the cloud column, the control simulation demonstrates good agreement with median
551 observation values to within ~2-3 dB. The observed PSD and Z_{Ku} evolution with height support a
552 precipitation evolution pathway described by robust production or concentration of ice within the
553 updraft region of the generating cell layer along the frontal boundary aloft (~5.5 km a.m.s.l.) and
554 fallout within the downdraft regions below. This agreeing result establishes confidence in the
555 quasi-idealized 1D control simulation and, crucially, the simulated microphysical processes
556 within their ambient environment, prescriptively constrained by in situ measurements.

557 Microphysical evolution between the generating cell layer at 5.5 km a.m.s.l. and 3.6 km
558 a.m.s.l. was dominated by sublimation, yielding a significant IWC loss. Riming, whether within
559 isolated regions of updrafts or following sublimation (i.e., Fig. 4, 17:10:05 UTC), negated some
560 of the ice mass loss, as supported by the rime fractional mass of 0.33 accumulated at 3.6 km
561 a.m.s.l. in the control simulation. Further, riming likely aided fallout through increases in particle
562 density, and subsequently fall speed. As a result, when assessed as the vertical mass flux at 3.6



563 km a.m.s.l. (lowest altitude of P-3 observations), the control simulation produced a liquid-
564 equivalent rain rate of 0.66 mm h^{-1} . When compared to measurements at KIWI, which reported
565 1.02 mm during the 17:00 UTC hour, at the time of aircraft overpass on flight leg 5 (Fig. 2), the
566 control simulation appears to underestimate the precipitation rate. However, the model does not
567 account for liquid-phase precipitation which may have formed below the melting level.
568 Additionally, the surface precipitation rate at KIWI during the following 18:00 UTC hour
569 reduced to 0.76 mm h^{-1} , in better agreement with the simulation. Despite the subsaturated
570 ambient environment, precipitation fallout was maintained through the cloud contributing to a
571 relative enhancement in surface precipitation rate with passage of the band.

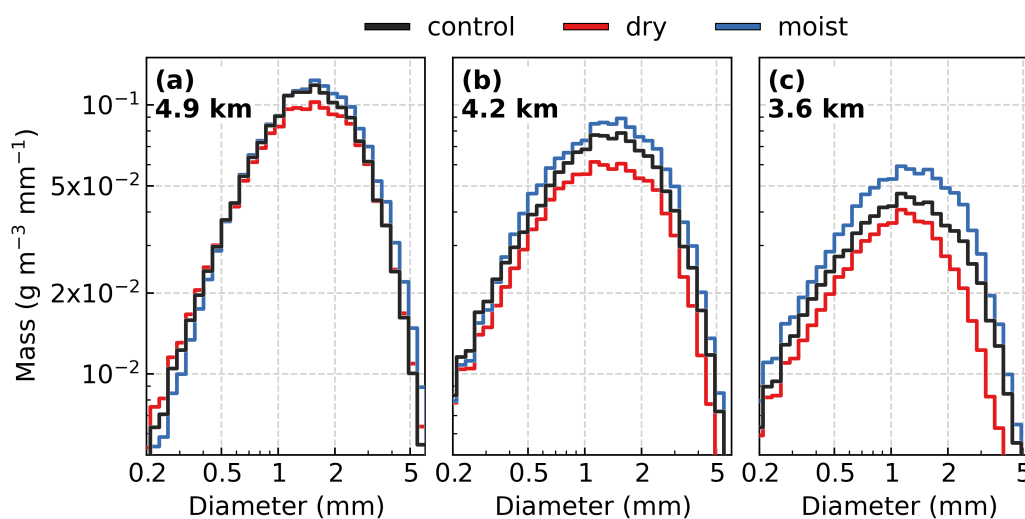
572

573 **5. Ambient controls on particle evolution**

574 The frontal cloud exhibited a heterogeneity expressed in the diversity of ice crystal habits and
575 their apparent process-based evolution (e.g., sublimation and riming, Fig. 4) and similarly, in the
576 ambient RH (Fig. 6a) and the magnitude and direction of vertical winds below $\sim 5 \text{ km a.m.s.l.}$
577 (Fig. 7). Despite the promising agreement between our control simulation and the observations, a
578 limiting assumption of the simulation is the reduction of the natural cloud's heterogeneity to a
579 prescriptive median state ambient environment. We are, therefore, motivated to explore the
580 particle evolution within perturbed ambient environments constrained by the range of variability
581 observed in the natural cloud. In considering precipitation pathways within these perturbed
582 environments, we further aim to elucidate the ambient dependencies of the dominant
583 microphysical process and quantify those effects on surface precipitation. Because the dominant
584 microphysical processes acting on particles upon fallout from the generating cell layer were
585 sublimation and sedimentation, we perturb two properties of the ambient environment that



586 directly affect these processes and demonstrated a range of variability in the natural cloud, RH
587 and w (i.e., updrafts and downdrafts). From these ambient properties, two groups of sensitivity
588 simulations are designed from the interquartile ranges of in situ measurements (Figs. 6a and 7).
589
590



591

592 **Figure 10:** Ice mass PSDs for the control, dry, and moist simulations at (a) 4.9 km a.m.s.l.
593 corresponding to P-3 flight leg 3, (b) 4.2 km a.m.s.l. corresponding to P-3 flight leg 4, and (c) 3.6
594 km a.m.s.l. corresponding to P-3 flight leg 5. Perturbed-state cloud RH profiles for the dry and
595 moist simulations are derived from the interquartile range of in situ observations (see Fig. 6a).
596

597 **5.1. Ambient relative humidity**

598 For simulations which we term “dry” and “moist”, the prescriptive cloud moisture input is
599 perturbed by assuming the 25th and 75th percentile values of observed RH (Fig. 6a). For both the
600 dry (25th percentile) and moist (75th percentile) simulations, most perturbations at all heights
601 were $< 2\%$ RH, with the largest perturbation being a decrease of 2.6% RH at 4.9 km a.m.s.l. in
602 the dry simulation and increase of 2.9% RH at 3.6 km a.m.s.l. in the moist simulation. Figure 10
603 shows the simulated PSD for the control, dry, and moist simulations. Although retrievable at any



604 height from the simulation, we found it convenient to assess the PSD at heights equivalent to P-3
605 flight legs 3 through 5. At 5.5 km a.m.s.l. (flight leg 2), where particles are initialized,
606 simulations do not meaningfully differ from each other. Between 4.9 and 3.6 km a.m.s.l. (Fig.
607 10a-c), all simulations reproduce the reduction of IWC with descent; however, the extent of loss
608 among all particle sizes is modulated by ambient RH. Table 1 quantitatively summarizes the
609 IWC at each height for the control and sensitivity simulations. At 3.6 km a.m.s.l., IWC is further
610 reduced from the control simulation by ~26% in the dry simulation and increased by ~29% in the
611 moist simulation. Because of the significant effects of sublimational ice losses identified in the
612 control simulation, it is perhaps unsurprising that small perturbations ($< \sim 2\%$ RH) in the dry and
613 moist simulation yield increasing departures from the control with descent. Nonetheless, these
614 simulations demonstrate a significant dependency on ambient RH for the survival of ice mass
615 falling through the ~2 km deep subsaturated cloud layer.

616

617

height	control	dry	moist	downdraft	updraft
5.5 km a.m.s.l.	0.606	0.600 [0%]	0.621 [+2.5%]	0.619 [+2.1%]	0.630 [+4.0%]
4.9 km a.m.s.l.	0.303	0.287 [-5.3%]	0.337 [+11.2%]	0.298 [-1.7%]	0.331 [+9.2%]
4.2 km a.m.s.l.	0.214	0.168 [- 21.5%]	0.247 [+15.4%]	0.207 [-3.3%]	0.207 [-3.3%]
3.6 km a.m.s.l.	0.119	0.088 [- 26.1%]	0.154 [+29.4%]	0.116 [-2.5%]	0.118 [-0.1%]

618 **Table 1:** Simulated IWC (g m^{-3}) at heights equivalent to the P-3 aircraft on flight legs 2
619 through 5 for the control, dry, moist, downdraft, and updraft sensitivity simulations. Perturbed-
620 state cloud RH profiles for the dry and moist simulations are derived from the interquartile range
621 of in situ observations (see Fig. 6a). Perturbed-state cloud vertical wind profiles for the
622 downdraft and updraft simulations are derived from the interquartile range of in situ observations
623 (see Fig. 7).

624



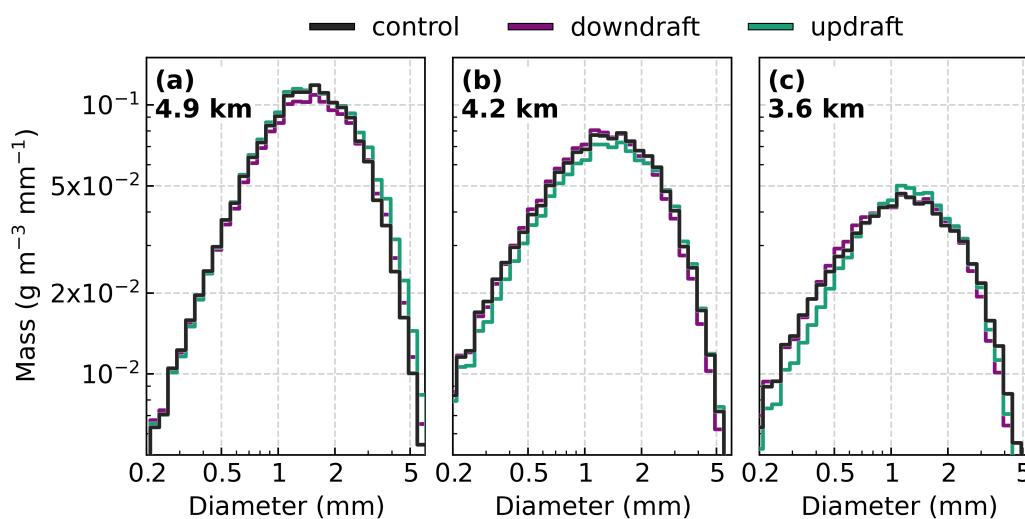
625 **5.2. Ambient vertical wind magnitude and direction**

626 As with the ambient RH, we introduce two sensitivity simulations termed “downdraft” and
627 “updraft” which perturb the prescriptive ambient w by assuming the 25th and 75th percentile
628 values of observations (Fig. 7). Perturbation at all heights for the downdraft (25th percentile)
629 simulation decreased w by $\sim 0.1 \text{ m s}^{-1}$, yielding reduced updrafts in the generating cell layer and a
630 stronger downdraft below. Conversely, perturbations at all heights in the updraft (75th percentile)
631 simulation similarly increased w by $\sim 0.1 \text{ m s}^{-1}$. This resulted in a completely ascending profile
632 throughout the cloud, albeit nearly static ($w = 0.01 \text{ m s}^{-1}$) at 4.2 km a.m.s.l. Even in this
633 perturbed state at the upper quartile of observations, w in the generating cell layer is 0.74 m s^{-1} ,
634 whereas updrafts greater than $\sim 1 \text{ m s}^{-1}$ may be more typical of a generating cell layer. Thus,
635 given our observationally-constrained design specific to the 4 February event, our sensitivity
636 simulations assess a relatively small range of possible updraft and downdraft magnitudes within
637 generating cell clouds producing fallout precipitation.

638 Figure 11 shows the evolved PSD for the control, downdraft, and updraft simulations.
639 Compared to RH, the evolved PSD demonstrates a reduced range of variation in response to the
640 w perturbations. Notably, the greatest differences between simulations manifest at small particle
641 sizes ($D < \sim 1 \text{ mm}$), which is a result of the differences in the particle’s intrinsic V_t as the
642 particles reach 3.6 km a.m.s.l. (Fig. 11c). In general, V_t increases with increasing particle size
643 (e.g., Locatelli and Hobbs, 1974). Thus, small particles have a relatively small intrinsic V_t and
644 when subject to a small perturbation in w ($\sim 0.1 \text{ m s}^{-1}$), experience an outsized net effect relative
645 to larger, faster falling particles. For example, at 3.6 km a.m.s.l. in the control simulation, 0.2
646 mm diameter particles attained a V_t of -0.42 m s^{-1} , whereas 2 mm particles had a V_t of -1.39 m s^{-1} .
647 ¹. Because ice mass is dominated by the larger, faster falling particles, which were minimally



648 affected by w perturbations, the IWC in the downdraft and updraft simulation at 3.6 km a.m.s.l.
649 were strikingly similar to the control simulation (within 2.5%).
650
651



652

653 **Figure 11:** Ice mass PSDs for the control, downdraft, and updraft simulations at (a) 4.9 km
654 a.m.s.l. corresponding to P-3 flight leg 3, (b) 4.2 km a.m.s.l. corresponding to P-3 flight leg 4,
655 and (c) 3.6 km a.m.s.l. corresponding to P-3 flight leg 5. Perturbed-state cloud vertical wind
656 profiles for the downdraft and updraft simulations are derived from the interquartile range of in
657 situ observations (see Fig. 7).
658

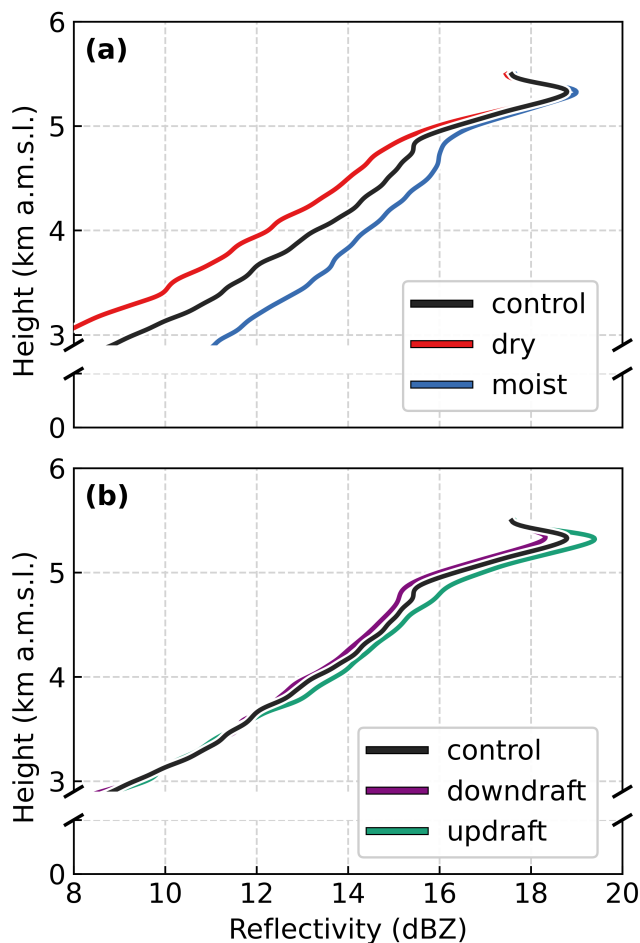
659 The most notable influence of w on IWC occurs in the updraft simulation at 4.9 km a.m.s.l.
660 (~9% increase, Table 1). This local enhancement is likely due to the enhanced lofting and
661 concentrating of particles which must overcome a larger w in the updraft region immediately
662 above the 4.9 km a.m.s.l. evaluation height. However, any resultant enhancement in IWC from
663 additional lofting within the updraft region appears to be negated between 4.9 and 3.6 km a.m.s.l.
664 by the outsized effect of sublimational ice loss among all particle sizes. While the updraft within
665 the generating cell layer is crucial to the production and maintenance of a relatively high IWC



666 aloft, perturbations of w in either the updraft or downdraft regions yielded an inconsequential net
667 effect on IWC 3.6 km a.m.s.l. However, the sedimentation rate of particles is modified by w
668 perturbations. For example, a 2 mm particle's sedimentation rate at 3.6 km a.m.s.l. in the
669 downdraft simulation was -1.52 m s^{-1} , whereas in the updraft simulation, the rate slowed to -1.36
670 m s^{-1} . The ice-phase contribution to surface precipitation rates is governed by IWC, which has an
671 evolutionary sensitivity to ambient RH (Fig. 10), and its sedimentation rate, which is modified
672 by w . Because of the dependency on radar remote sensing measurements to estimate
673 precipitation rates and the diverse process-based outcomes from these ambient perturbations, we
674 next quantify these effects on vertical profiles of Z_{Ku} and $V_{D_{Ku}}$.

675

676



677

678 **Figure 12:** Ku-band radar reflectivity profiles for the (a) dry- and moist-perturbed and (b)
679 updraft- and downdraft-perturbed sensitivity simulations relative to the control simulation.
680

681 **5.3. Implications of process-based responses to ambient variabilities on radar remote** 682 **sensing measurements**

683 During the 4 February event, the enhancement in the composite reflectivity field along the
684 band was a sustained, prominent feature that suggested a local enhancement in surface
685 precipitation (Fig. 1). However, from vertical radar profiles across the band (e.g., Fig. 2), within



686 the ice layer there was a relative maximum in Z_{Ku} at the generating cell layer, which weakened
687 with descent in the fallout layer below. The more substantial maxima in column Z_{Ku} occurred
688 from melting near 3 km a.m.s.l. For the ice-phase precipitation aloft, this signature of Z_{Ku}
689 reduction with descent is a result of sublimational loss and an inefficient aggregation process,
690 which was supported by results of the control simulation. These losses through the cloud have
691 implications for the downward precipitation mass flux, and therefore, precipitation rates at the
692 surface. Thus, by quantifying the effects of process-based evolutionary responses to perturbed
693 ambient environments, we aim to determine the utility of remote sensing radar measurements to
694 discern ice-phase microphysical processes and their implications for precipitation mass and its
695 fallout.

696 Vertical profiles of Z_{Ku} estimated from the evolving PSD between 5.5 and 3 km a.m.s.l. are
697 shown in Fig. 12 for the control and sensitivity experiments. All simulations produce a relative
698 maximum in Z_{Ku} immediately below initialization at 5.5 km a.m.s.l. associated with the updraft
699 and concentration of ice mass followed by a continuous reduction in Z_{Ku} with descent thereafter,
700 which is consistent with the observations (Fig. 9). A distinct change in the rate of change in Z_{Ku}
701 with height occurs at 5 km a.m.s.l. as a result of the initial onset of riming. Below 5 km a.m.s.l.,
702 Z_{Ku} in the RH-perturbed environments becomes increasingly differentiated from the control with
703 descent (Fig. 12a). At 3.6 km a.m.s.l., Z_{Ku} was reduced in the dry simulation by 1.5 dB (~12 %)
704 and increased in the moist simulation by 1.6 dB (~13%) relative to the control (Table 2). To
705 provide context for these results, we estimate the liquid-equivalent precipitation rate at 3.6 km
706 a.m.s.l. Reducing RH by ~1 to 2% in the dry simulation yielded a precipitation rate decrease of
707 ~24%, whereas similarly increasing RH yielded a precipitation rate increase of ~33% (Table 2).
708 Thus, modification of precipitation rate owed to differential ice losses by sublimation as a result



709 of perturbed RH below the generating cell layer has a direct implication on the rate of change in
 710 Z_{Ku} with height. Perturbations in w produced a greater range of Z_{Ku} variation aloft, within the
 711 updraft region, although, by 3.6 km a.m.s.l., the downdraft and updraft simulations are nearly
 712 indistinguishable from the control (Fig. 12b). Similarly, the precipitation rate at 3.6 km a.m.s.l. is
 713 not meaningfully affected by perturbation in w (Table 2).

714

715

height	property	control	dry	moist	downdraft	updraft
5.5 km a.m.s.l.	reflectivity (dBZ)	18.0	17.8 [-1.1%]	18.2 [+1.1%]	18.1 [+0.6%]	18.4 [+2.2%]
4.9 km a.m.s.l.	reflectivity (dBZ)	15.7	15.3 [-2.5%]	16.1 [+2.5%]	15.3 [-2.5%]	16.4 [+4.5%]
4.2 km a.m.s.l.	reflectivity (dBZ)	14.3	13.0 [-9.1%]	15.0 [+4.9%]	13.9 [-2.8%]	14.5 [+1.4%]
3.6 km a.m.s.l.	reflectivity (dBZ)	12.2	10.7 [-12.3%]	13.8 [+13.1%]	11.6 [-4.9%]	12.4 [+1.7%]
3.6 km a.m.s.l.	precipitation rate (mm h ⁻¹)	0.66	0.50 [-24.2%]	0.88 [+33.3%]	0.65 [-1.5%]	0.63 [-4.5%]

716 **Table 2:** Simulated Ku-band radar reflectivity at heights equivalent to the P-3 aircraft on
 717 flight legs 2 through 5 and liquid-equivalent precipitation rate at flight leg 5 for the control, dry,
 718 moist, downdraft, and updraft sensitivity simulations. Perturbed-state cloud RH profiles for the
 719 dry and moist simulations are derived from the interquartile range of in situ observations (see
 720 Fig. 6a). Perturbed-state cloud vertical wind profiles for the downdraft and updraft simulations
 721 are derived from the interquartile range of in situ observations (see Fig. 7).

722

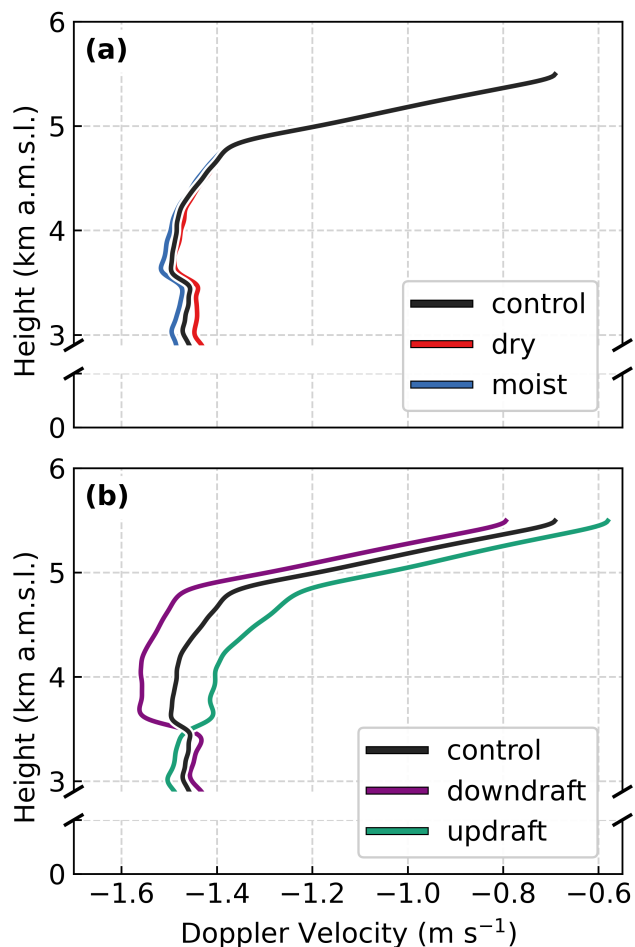
723 The insensitivity of precipitation rate to perturbations in w indicates that precipitation flux
 724 through the subsaturated ice layer is more strongly governed by the IWC preserved throughout
 725 the layer than by changes in the sedimentation rate of the ice particles. This principle is similarly
 726 expressed by the simulated vertical profiles of $V_{D_{Ku}}$ (Fig. 13). Whereas, relative to the control
 727 simulation, perturbations in RH produced substantial differentiation in Z_{Ku} and, ultimately,



728 precipitation rate at 3.6 km a.m.s.l., a much smaller range of differentiation occurs for V_{D_Ku} (Fig.
729 13a). At 3.6 km a.m.s.l., V_{D_Ku} in the dry and moist simulations are within 0.02 m s^{-1} of the
730 control simulation (-1.51 m s^{-1}). Similarly, while the updraft and downdraft simulations appear to
731 produce V_{D_Ku} profiles that are distinct from the control (Fig. 13b), the magnitude of difference
732 throughout the ice layer is explained by the magnitude of perturbation in w rather than a change
733 in the particles intrinsic V_t through perturbed microphysical evolution.

734

735



736

737

738 **Figure 13:** Radar Doppler velocity profiles for the (a) dry- and moist-perturbed and (b)
739 updraft- and downdraft-perturbed sensitivity simulations relative to the control simulation at Ku-
740 band.

741

742 6. Discussion

743 Despite the decaying stage of the winter storm, modest yet locally enhanced surface

744 precipitation rates ($\sim 1 \text{ mm h}^{-1}$) were sustained at the banded region by precipitation fallout from

745 the relatively high median IWC (0.540 g m^{-3}) in the generating cell layer. Within updraft regions



746 of generating cell layers, airborne observations have revealed enhancements in IWC (e.g., Houze
747 et al., 1981; Plummer et al., 2015) and LWC (e.g., Wolde and Vali, 2001; Evans et al., 2005;
748 Ikeda et al., 2007; Plummer et al., 2014). These generating cell layers are therefore a source
749 region for significant precipitation enhancements in ambient environments supportive of particle
750 growth in the fallout region below. Indeed, prior studies have found that a majority of IWC
751 accumulation occurs below generating cell layers through vapor deposition and aggregation (e.g.,
752 Herzegh and Hobbs, 1980; Plummer et al., 2015); two processes that were notably absent in the
753 fallout region of the banded cloud on 4 February. Thus, contrasting with the precipitation
754 pathways more commonly associated with generating cells, the dominant microphysical process
755 between the generating cell layer and the melting level was sublimation, which yielded a
756 substantial (> 70%) loss of IWC.

757 The primary determinant for the rate of precipitation fallout from the banded cloud
758 contributing to surface enhancements was the amount of ice mass preserved through the
759 subsaturated layer. Sensitivity simulations demonstrated that, within this subsaturated
760 environment, particle evolution and its fallout have strong dependencies on the ambient RH (Fig.
761 10) but weak dependencies on w (Fig. 11) when independently assessed over an equivalent range
762 of observed variation. The intrinsic evolution of particle V_i during sublimation and, subsequently,
763 riming contributes an outsized effect on precipitation fallout relative to perturbations of the
764 ambient w , which affect the sedimentation rate. Nonetheless, the w profile being characterized by
765 a median state updraft in the generating cell layer and intermittent updraft regions within overall
766 descent below were necessary in establishing conditions favorable for the riming that was
767 observed in particle imagery. Although riming was not evident among particles within the
768 generating cell layer at 5.5 km a.m.s.l., rimed particles were prevalent at 4.9 km a.m.s.l. and



769 below, albeit heterogeneously distributed. Provided by a supply of supercooled liquid water in
770 updraft regions, riming is an efficient growth process for precipitation within and below the
771 generating cell (e.g., Houze et al., 1981; Plummer et al., 2014; Kumjian et al., 2014). Rime
772 accumulation appears to have had a prominent effect on IWC. In the control run simulation,
773 approximately 33% of the IWC at 3.6 km a.m.s.l. was attributable to rime accumulation. This
774 contribution may even be underrepresented by the model based on the smaller IWC in the
775 simulation at 3.6 km a.m.s.l. and the increase in IWC from 4.2 to 3.6 km a.m.s.l. in the
776 observations which was not reproduced in the simulation.

777 The resultant microphysical evolutionary pathways for particles within the banded region and
778 the southerly displaced region of enhanced reflectivity (Fig. 1) substantially differ. Riming was
779 prevalent in both regions, but to varied degrees. In the southern region, DeLaFrance et al.
780 (2024b) identified robust particle growth by widespread riming which was enhanced by a highly
781 efficient, concurrent aggregation process. Consequently, despite a similar but reduced magnitude
782 of composite reflectivity (Fig. 1), simulated precipitation rates in the southern region were over
783 two and a half times greater (1.77 mm h^{-1}) than those simulated for the banded region (0.66 mm
784 h^{-1}). These differences are demonstrative of the implications of process-based modulation of
785 microphysical properties, which remain challenging to constrain in remote sensing retrievals, and
786 underscores the need for ice-phase process discrimination in radar measurements.

787 In the present study, sensitivity simulations were used to quantify the imprint of sublimation
788 on vertical profiles of Z_{Ku} and V_{D_Ku} . We found that vertical profiles of Z_{Ku} demonstrate a
789 substantial sensitivity (~ 12 to 13% dB) to varied rates of sublimational IWC loss from perturbed
790 RH environments (Fig. 12, Table 2) whereas V_{D_Ku} is relatively insensitive to these perturbations
791 (Fig. 13). Perturbations in w increase or decrease the magnitude of V_{D_Ku} , but the rate of V_{D_Ku}



792 was dominated by the significantly greater median-state magnitude differences between the
793 updraft and downdraft regions. Whereas V_{D_Ku} was previously shown to be especially sensitive to
794 riming-based variabilities (DeLaFrance et al., 2024b), in the present study, it provided no
795 independent quantitative value towards differentiating effects of sublimation (Fig. 13). Although
796 not evaluated here, this finding likely extends to differentiation of the effects of depositional
797 growth, but for increasing Z_{Ku} with descent. In this scenario, an equivalent sensitivity of Z_{Ku} but
798 not V_{D_Ku} to depositional growth is analogous to the effects of aggregation (DeLaFrance et al.,
799 2024b). A similar ambiguity in the process-based distinction between depositional growth and
800 aggregation exists for multi-frequency radar techniques as scattering models have shown
801 dendritic and complex aggregation particles occupy a similar dual- and triple-frequency radar
802 scattering signatures (e.g., Petty and Huang, 2010; Kneifel et al., 2011; Leinonen and Moisseev,
803 2015). Thus, discrimination between either low-density dendritic or complex aggregate particle
804 types or between deposition- or aggregation-dominant growth from remote sensing
805 measurements is likely to remain a challenge.

806

807 **7. Conclusions**

808 Mesoscale band development within winter storms is typically accompanied by
809 enhanced, and often, high-impact, surface precipitation rates over confined regions. The
810 microphysical properties of the ice-phase particles within these banded regions remain poorly
811 represented by numerical models and challenging to constrain in radar remote sensing retrievals,
812 owed in part to an incomplete understanding of the diverse microphysical pathways for banded
813 precipitation evolution. Addressing a need for more observations within natural clouds, the
814 IMPACTS campaign deployed a cloud-penetrating P-3 and overflying ER-2 aircraft to measure



815 properties of a mesoscale banded region of a northeastern U.S. winter storm on 4 February 2022.
816 During the ~3 h period that IMPACTS executed Lagrangian sampling of the banded region, the
817 storm exhibited an apparent state of decay, weakening in composite radar reflectivity intensity,
818 yet maintaining a banded structure. This paper aimed to characterize the evolutionary pathways
819 for precipitation within the decaying-stage banded region, assess those implications for surface
820 precipitation, quantify sensitivities to ambient environmental properties, and determine the
821 imprint of microphysical process-based evolution on radar remote sensing measurements.

822 Surface precipitation along the band was associated with clouds that formed along a
823 stationary frontal boundary having a weak generating cell layer from ~6 to 5 km a.m.s.l. ($w =$
824 $\sim 0.6 \text{ m s}^{-1}$) and precipitation fallstreaks between ~5 km a.m.s.l. and the melting level, near 3 km
825 a.m.s.l. The fallout region between the generating cell layer and melting level was characterized
826 by a weak downdraft ($w < \sim -0.1 \text{ m s}^{-1}$) and subsaturated ($\text{RH} = \sim 80$ to 83%) ambient
827 environment. Particle imagery at all heights showed evidence of sublimation; however, riming
828 was also present in heterogeneously distributed regions of a mixed-phase layer extending to ~5
829 km a.m.s.l. We observed very little evidence of aggregation.

830 Quasi-idealized 1D model simulations using the Lagrangian particle-based McSnow
831 model were designed from observational constraints with prescriptive ambient environments.
832 The observed reduction in IWC, particle sizes, and Z_{Ku} with descent through the ~2 km deep
833 fallout layer were reasonably reproduced by the control simulation and provided confidence in
834 the modeled representation of precipitating particle evolution within the natural cloud. We
835 designed four sensitivity simulations to elucidate evolutionary dependencies on ambient cloud
836 moisture and vertical air motions based on perturbations in the prescribed RH and w profiles
837 defined by the IQR of variability. From these sensitivity simulations, we quantified sensitivities



838 of particle growth and decay to ambient environmental properties and estimated downward mass
839 flux to determine the implications on precipitation fallout within the banded region. Finally,
840 these sensitivity simulations were used to determine the process-based imprint on remote sensing
841 measurements of Z_{Ku} and V_{D_Ku} within this unique environment of the decay-state banded cloud.
842 Collectively, the control simulation and four sensitivity simulations have supported the following
843 conclusions:

844

- 845 ○ Enhanced surface precipitation rates during the passage of the mesoscale band resulted
846 from relatively high IWC formed within a generating cell layer that produced ice-phase
847 precipitation fallout within a descending layer below the generating cells.
- 848 ○ The ambient environment of the frontal cloud supported a dominant ice-phase
849 microphysical evolution by sublimation, and secondarily, riming processes to yield a net
850 IWC loss exceeding 70% within the subsaturated fallout layer.
- 851 ○ Perturbations in ambient RH (~2%) yielded a substantial change in IWC preserved
852 throughout the subsaturated layer (-26% to 29%) and in liquid-equivalent precipitation
853 rate (-24% to 33%); relative to RH, w -based perturbations (~0.1 m s⁻¹) yielded
854 substantially decreased range of variability in IWC (< 2.5%) and precipitation rate (<
855 4.5%).
- 856 ○ Vertical profiles of Z_{Ku} were strongly dependent on RH-perturbed rates of sublimational
857 IWC loss throughout the cloud, but dependent on w -perturbed sedimentation rates only in
858 the updraft region; vertical profiles of V_{D_Ku} demonstrated negligible microphysical
859 process-based sensitivity.

860



861 The 4 February 2022 winter storm event provided a unique natural laboratory for assessing
862 process-based implications for ice-phase precipitation evolutionary pathways within winter
863 storms for several reasons. The winter storm was characterized by two distinct regions of
864 enhanced reflectivity with diverse surface precipitation rates owed to their unique microphysical
865 pathways. These regions were well sampled by aircraft during the IMPACTS field campaign,
866 providing crucial coincident in situ and remote sensing measurements with approximately
867 Lagrangian spatial and temporal context. The southern region of enhanced reflectivity, which
868 lacked well-defined banding, experienced sustained particle growth above the melting level
869 dominated by riming (DeLaFrance et al., 2024b). The banded region to the north was more
870 strongly affected by the decaying stage of the storm from an intrusion of subsaturated air
871 throughout the ice-phase layer of cloud. Consequently, particle growth was unsupported by the
872 ambient environment of the banded region and ice loss through sublimation was a dominant
873 microphysical pathway. For each region, the storm's natural characteristics supported the
874 isolation of a microphysical process (i.e., riming or sublimation) in modeling sensitivity
875 simulations to assess their unique implications for surface precipitation and sensitivities to
876 ambient environmental properties. Results presented in the present study and DeLaFrance et al.
877 (2024b) provide new quantitative insights on the imprint of microphysical processes on radar
878 remote sensing measurements with application towards future retrieval algorithm development,
879 especially among those incorporating Doppler velocity measurements. Additionally, these
880 studies provide a framework of observational constraint and validation in future quasi-idealized
881 Lagrangian and particle-based modeling studies to further quantify the unique implications of
882 process-based microphysical evolution within diverse winter storm environments.

883



884

885 **Code and data availability**

886 IMPACTS data are publicly available through the NASA Distributed Active Archive Center
887 (<https://doi.org/10.5067/IMPACTS/DATA101>, McMurdie et al., 2019). Specific IMPACTS
888 datasets used for analysis include NCAR Particle Probes
889 (<https://doi.org/10.5067/IMPACTS/PROBES/DATA101>, Bansemmer et al., 2022), Particle Habit
890 Imaging and Polar Scattering Probe (<http://doi.org/10.5067/IMPACTS/PHIPS/DATA101>,
891 Schnaiter, 2022), P-3 Meteorological and Navigation Data
892 (<https://doi.org/10.5067/IMPACTS/P3/DATA101>, Yang-Martin and Bennett, 2022), Automated
893 Surface Observing System (<https://doi.org/10.5067/IMPACTS/ASOS/DATA101>, Brodzik,
894 2022a), High Altitude Imaging Wind and Rain Airborne Profiler
895 (<https://doi.org/10.5067/IMPACTS/HIWRAP/DATA101>, McLinden et al., 2022), Turbulent Air
896 Motion Measurement System (<https://doi.org/10.5067/IMPACTS/TAMMS/DATA101>,
897 Thornhill, 2022), Multi-Radar/Multi-Sensor (MRMS) Precipitation Reanalysis for Satellite
898 Validation Product (<https://doi.org/10.5067/IMPACTS/MRMS/DATA101>, Brodzik, 2022b), and
899 NOAA Soundings (<https://doi.org/10.5067/IMPACTS/SOUNDING/DATA201>, Waldstreicher
900 and Brodzik, 2022).

901

902

903

904 **Author contributions**

905 All authors contributed to decisions on methodologies applied throughout the study. AD
906 performed the data analysis, modeling simulations, and processing of the model output. All the
907 authors contributed to interpretations and assessed implications of the results. AD prepared the
908 manuscript with contributions from all the co-authors.

909

910

911 **Competing interests**

912 The contact author has declared that none of the authors has any competing interests.

913

914

915 **Acknowledgements**

916 The authors acknowledge the IMPACTS team for their dedicated efforts in the collection and
917 curation of the unique and exceptionally high-quality IMPACTS dataset. The authors also thank
918 Aaron Bansemmer for several helpful discussions regarding the interpretations and limitations of
919 the processed microphysics probe data. Andrew DeLaFrance acknowledges NCAR for resources
920 provided to visit its Mesoscale and Microscale Meteorology Laboratory (host Andrew J.
921 Heymsfield), supporting the initial study conceptualization and design.

922

923

924 **Financial support**

925 This research was supported by the National Aeronautics and Space Administration (grant nos.
926 80NSSC21K1589, 80NSSC19K0338, and 80NSSC19K0397). Andrew J. Heymsfield is
927 supported by the National Science Foundation.

928



929 **References**

- 930 Bansemmer, A., Delene, D., Heymsfield, A., and O'Brien, J.: NCAR Particle Probes IMPACTS,
931 Dataset available online from the NASA Global Hydrometeorology Resource Center
932 DAAC, Huntsville, Alabama, USA [data set],
933 <https://doi.org/10.5067/IMPACTS/PROBES/DATA101>, 2022.
- 934 Boucher, R. J. and Wieler, J. G.: Radar Determination of Snowfall Rate and Accumulation, J.
935 Appl. Meteorol. Clim., 24, 68–73, [https://doi.org/10.1175/1520-0450\(1985\)024<0068:RDSRA>2.0.CO;2](https://doi.org/10.1175/1520-0450(1985)024<0068:RDSRA>2.0.CO;2), 1985.
- 937 Bringi, V., Seifert, A., Wu, W., Thurai, M., Huang, G.-J., and Siewert, C.: Hurricane Dorian
938 Outer Rain Band Observations and 1D Particle Model Simulations: A Case Study,
939 Atmosphere, 11, 879, <https://doi.org/10.3390/atmos11080879>, 2020.
- 940 Brodzik, S.: Automated Surface Observing System (ASOS) IMPACTS, Dataset available online
941 from the NASA Global Hydrometeorology Resource Center DAAC, Huntsville,
942 Alabama, USA [data set], <https://doi.org/10.5067/IMPACTS/ASOS/DATA101>, 2022a.
- 943 Brodzik, S.: Multi-Radar/Multi-Sensor (MRMS) Precipitation Reanalysis for Satellite Validation
944 Product IMPACTS, Dataset available online from the NASA Global Hydrometeorology
945 Resource Center DAAC, Huntsville, Alabama, USA [data set],
946 <https://doi.org/10.5067/IMPACTS/MRMS/DATA101>, 2022b.
- 947 Brown, P. R. A. and Francis, P. N.: Improved Measurements of the Ice Water Content in Cirrus
948 Using a Total-Water Probe, J. Atmos. Ocean. Tech., 12, 410–414,
949 [https://doi.org/10.1175/1520-0426\(1995\)012<0410:IMOTIW>2.0.CO;2](https://doi.org/10.1175/1520-0426(1995)012<0410:IMOTIW>2.0.CO;2), 1995.
- 950 Chase, R. J., Nesbitt, S. W., and McFarquhar, G. M.: Evaluation of the Microphysical
951 Assumptions within GPM-DPR Using Ground-Based Observations of Rain and Snow,
952 Atmosphere, 11, 619, <https://doi.org/10.3390/atmos11060619>, 2020.
- 953 Chase, R. J., Nesbitt, S. W., McFarquhar, G. M., Wood, N. B., and Heymsfield, G. M.: Direct
954 Comparisons between GPM-DPR and CloudSat Snowfall Retrievals, J. Appl. Meteor.
955 Clim., 61, 1257–1271, <https://doi.org/10.1175/JAMC-D-21-0081.1>, 2022.
- 956 Colle, B. A., Stark, D., and Yuter, S. E.: Surface Microphysical Observations within East Coast
957 Winter Storms on Long Island, New York, Mon. Weather Rev., 142, 3126–3146,
958 <https://doi.org/10.1175/MWR-D-14-00035.1>, 2014.
- 959 Colle, B. A., Yeh, P., Finlon, J. A., McMurdie, L., McDonald, V., and DeLaFrance, A.: An
960 Investigation of a Northeast U.S. Cyclone Event without Well-Defined Snow Banding
961 during IMPACTS, Mon. Weather Rev., 151, 2465–2484, <https://doi.org/10.1175/MWR-D-22-0296.1>, 2023.
- 963 Connolly, P. J., Emersic, C., and Field, P. R.: A Laboratory Investigation into the Aggregation
964 Efficiency of Small Ice Crystals, Atmos. Chem. Phys., 12, 2055–2076,
965 <https://doi.org/10.5194/acp-12-2055-2012>, 2012.
- 966 DeLaFrance, A., McMurdie, L. A., Rowe, A. K., and Conrick, R.: Effects of Riming on Ice-
967 Phase Precipitation Growth and Transport Over an Orographic Barrier, J. Adv. Model
968 Earth Syst., 16, e2023MS003778, <https://doi.org/10.1029/2023MS003778>, 2024a
- 969 DeLaFrance, A., McMurdie, L. A., Rowe, A. K., and Heymsfield, A. J.: Simulated Particle
970 Evolution Within a Winter Storm: Contributions of Riming to Radar Moments and
971 Precipitation Fallout, Atmos. Chem. Phys., 24, 11191–11206,
972 <https://doi.org/10.5194/acp-24-11191-2024>, 2024b.
- 973 Dunnavan, E. L., Carlin, J. T., Schwartzman, D., Ryzhkov, A. V., Bluestein, H., Emmerson, S.,
974 McFarquhar, G. M., Heymsfield, G. M., and Yorks, J.: High-Resolution Snowstorm



- 975 Measurements and Retrievals Using Cross-Platform Multi-Frequency and Polarimetric
976 Radars, *Geophys. Res. Lett.*, 50, e2023GL103692,
977 <https://doi.org/10.1029/2023GL103692>, 2023.
- 978 Evans, A. G., Locatelli, J. D., Stoelinga, M. T., and Hobbs, P. V.: The IMPROVE-1 Storm of 1–
979 2 February 2001. Part II: Cloud Structures and the Growth of Precipitation, *J. Atmos.*
980 *Sci.*, 62, 3456–3473, <https://doi.org/10.1175/JAS3547.1>, 2005.
- 981 Finlon, J. A., McMurdie, L. A., and Chase, R. J.: Investigation of Microphysical Properties
982 within Regions of Enhanced Dual-Frequency Ratio during the IMPACTS Field
983 Campaign, *J. Atmos. Sci.*, 79, 2773–2795, <https://doi.org/10.1175/JAS-D-21-0311.1>,
984 2022.
- 985 Fujiyoshi, Y., Endoh, T., Yamada, T., Tsuboki, K., Tachibana, Y., and Wakahama, G.:
986 Determination of a $Z - R$ Relationship for Snowfall Using a Radar and High Sensitivity
987 Snow Gauges, *J. Appl. Meteorol.*, 29, 147–152, [https://doi.org/10.1175/1520-
988 0450\(1990\)029<0147:DOARFS>2.0.CO;2](https://doi.org/10.1175/1520-0450(1990)029<0147:DOARFS>2.0.CO;2), 1990.
- 989 Ganetis, S. A., Colle, B. A., Yuter, S. E., and Hoban, N. P.: Environmental Conditions
990 Associated with Observed Snowband Structures within Northeast U.S. Winter Storms,
991 *Mon. Weather Rev.*, 146, 3675–3690, <https://doi.org/10.1175/MWR-D-18-0054.1>, 2018.
- 992 Herzegh, P. H. and Hobbs, P. V.: The Mesoscale and Microscale Structure and Organization of
993 Clouds and Precipitation in Midlatitude Cyclones. II: Warm-Frontal Clouds, *J. Atmos.*
994 *Sci.*, 37, 597–611, [https://doi.org/10.1175/1520-
995 0469\(1980\)037<0597:TMAMSA>2.0.CO;2](https://doi.org/10.1175/1520-0469(1980)037<0597:TMAMSA>2.0.CO;2), 1980.
- 996 Heymsfield, A., Bansemer, A., Heymsfield, G., Noone, D., Grecu, M., and Toohey, D.:
997 Relationship of Multiwavelength Radar Measurements to Ice Microphysics from the
998 IMPACTS Field Program, *J. Appl. Meteorol. Clim.*, 62, 289–315,
999 <https://doi.org/10.1175/JAMC-D-22-0057.1>, 2023.
- 1000 Heymsfield, A. J. and Westbrook, C. D.: Advances in the Estimation of Ice Particle Fall Speeds
1001 Using Laboratory and Field Measurements, *J. Atmos. Sci.*, 67, 2469–2482,
1002 <https://doi.org/10.1175/2010JAS3379.1>, 2010.
- 1003 Heymsfield, A. J., Matrosov, S. Y., and Wood, N. B.: Toward Improving Ice Water Content and
1004 Snow-Rate Retrievals from Radars. Part I: X and W Bands, Emphasizing CloudSat,
1005 *J. Appl. Meteorol. Clim.*, 55, 2063–2090, <https://doi.org/10.1175/JAMC-D-15-0290.1>,
1006 2016.
- 1007 Houze, R. A., Rutledge, S. A., Matejka, T. J., and Hobbs, P. V.: The Mesoscale and Microscale
1008 Structure and Organization of Clouds and Precipitation in Midlatitude Cyclones. III: Air
1009 Motions and Precipitation Growth in a Warm-Frontal Rainband, *J. Atmos. Sci.*, 38, 639–
1010 649, [https://doi.org/10.1175/1520-0469\(1981\)038<0639:TMAMSA>2.0.CO;2](https://doi.org/10.1175/1520-0469(1981)038<0639:TMAMSA>2.0.CO;2), 1981.
- 1011 Ikeda, K., Rasmussen, R. M., Hall, W. D., and Thompson, G.: Observations of Freezing Drizzle
1012 in Extratropical Cyclonic Storms during IMPROVE-2, *J. Atmos. Sci.*, 64, 3016–3043,
1013 <https://doi.org/10.1175/JAS3999.1>, 2007.
- 1014 Jensen, A. A. and Harrington, J. Y.: Modeling Ice Crystal Aspect Ratio Evolution during
1015 Riming: A Single-Particle Growth Model, *J. Atmos. Sci.*, 72, 2569–2590,
1016 <https://doi.org/10.1175/JAS-D-14-0297.1>, 2015.
- 1017 Kalesse, H., Szyrmer, W., Kneifel, S., Kollias, P., and Luke, E.: Fingerprints of a Riming Event
1018 On Cloud Radar Doppler Spectra: Observations and Modeling, *Atmos. Chem. Phys.*, 16,
1019 2997–3012, <https://doi.org/10.5194/acp-16-2997-2016>, 2016.



- 1020 Keeler, J. M., Jewett, B. F., Rauber, R. M., McFarquhar, G. M., Rasmussen, R. M., Xue, L., Liu,
1021 C., and Thompson, G.: Dynamics of Cloud-Top Generating Cells in Winter Cyclones.
1022 Part I: Idealized Simulations in the Context of Field Observations, *J. Atmos. Sci.*, 73,
1023 1507–1527, <https://doi.org/10.1175/JAS-D-15-0126.1>, 2016.
- 1024 Kneifel, S., Kulie, M. S., and Bennartz, R.: A Triple-Frequency Approach to Retrieve
1025 Microphysical Snowfall Parameters, *J. Geophys. Res.-Atmos.*, 116, D11203,
1026 <https://doi.org/10.1029/2010JD015430>, 2011.
- 1027 Kneifel, S., Von Lerber, A., Tiira, J., Moisseev, D., Kollias, P., and Leinonen, J.: Observed
1028 Relations Between Snowfall Microphysics and Triple-Frequency Radar Measurements, *J.*
1029 *Geophys. Res.-Atmos.*, 120, 6034–6055, <https://doi.org/10.1002/2015JD023156>, 2015.
- 1030 Lawson, P., Gurganus, C., Woods, S., and Brientjes, R.: Aircraft Observations of Cumulus
1031 Microphysics Ranging from the Tropics to Midlatitudes: Implications for a “New”
1032 Secondary Ice Process, *J. Atmos. Sci.*, 74, 2899–2920, <https://doi.org/10.1175/JAS-D-17-0033.1>, 2017.
- 1034 Lawson, R. P., Stewart, R. E., Strapp, J. W., and Isaac, G. A.: Aircraft Observations of the Origin
1035 and Growth of Very Large Snowflakes, *Geophys. Res. Lett.*, 20, 53–56,
1036 <https://doi.org/10.1029/92GL02917>, 1993.
- 1037 Leinonen, J.: High-Level Interface to T-Matrix Scattering Calculations: Architecture,
1038 Capabilities and Limitations, *Opt. Express*, 22, 1655,
1039 <https://doi.org/10.1364/OE.22.001655>, 2014.
- 1040 Leinonen, J. and Moisseev, D.: What do Triple-Frequency Radar Signatures Reveal about
1041 Aggregate Snowflakes?, *J. Geophys. Res.-Atmos.*, 120, 229–239,
1042 <https://doi.org/10.1002/2014JD022072>, 2015.
- 1043 Leinonen, J. and Szyrmer, W.: Radar Signatures of Snowflake Riming: A Modeling Study, *Earth*
1044 *Space Sci.*, 2, 346–358, <https://doi.org/10.1002/2015EA000102>, 2015.
- 1045 Li, L., Heymsfield, G., Carswell, J., Schaubert, D. H., McLinden, M. L., Creticos, J., Perrine, M.,
1046 Coon, M., Cervantes, J. I., Vega, M., Guimond, S., Tian, L., and Emory, A.: The NASA
1047 High-Altitude Imaging Wind and Rain Airborne Profiler, *IEEE T. Geosci. Remote*, 54,
1048 298–310, <https://doi.org/10.1109/TGRS.2015.2456501>, 2016.
- 1049 Locatelli, J. D. and Hobbs, P. V.: Fall Speeds and Masses of Solid Precipitation Particles, *J.*
1050 *Geophys. Res.*, 79, 2185–2197, <https://doi.org/10.1029/JC079i015p02185>, 1974.
- 1051 Marshall, J. S. and Palmer, W. M. K.: The Distribution of Raindrops With Size, *J. Meteorol.*, 5,
1052 165–166, [https://doi.org/10.1175/1520-0469\(1948\)005<0165:TDORWS>2.0.CO;2](https://doi.org/10.1175/1520-0469(1948)005<0165:TDORWS>2.0.CO;2), 1948.
- 1053 Mason, S. L., Chiu, C. J., Hogan, R. J., Moisseev, D., and Kneifel, S.: Retrievals of Riming and
1054 Snow Density from Vertically Pointing Doppler Radars, *J. Geophys. Res.-Atmos.*, 123,
1055 13807–13834, <https://doi.org/10.1029/2018JD028603>, 2018.
- 1056 Mason, S. L., Hogan, R. J., Westbrook, C. D., Kneifel, S., Moisseev, D., and von Terzi, L.: The
1057 Importance of Particle Size Distribution and Internal Structure for Triple-Frequency
1058 Radar Retrievals of the Morphology of Snow, *Atmos. Meas. Tech.*, 12, 4993–5018,
1059 <https://doi.org/10.5194/amt-12-4993-2019>, 2019.
- 1060 Matrosov, S. Y., Korolev, A., Wolde, M., and Nguyen, C.: Sizing Ice Hydrometeor Populations
1061 Using the Dual-Wavelength Radar Ratio, *Atmos. Meas. Tech.*, 15, 6373–6386,
1062 <https://doi.org/10.5194/amt-15-6373-2022>, 2022.
- 1063 McLinden, M., Li, Lihua, and Heymsfield, Gerald M.: High Altitude Imaging Wind and Rain
1064 Airborne Profiler (HIWRAP) IMPACTS, Dataset available online from the NASA



- 1065 Global Hydrometeorology Resource Center DAAC, Huntsville, Alabama, USA [data
1066 set], <https://doi.org/10.5067/IMPACTS/HIWRAP/DATA101>, 2022.
- 1067 McMurdie, L. A., Heymsfield, G., Yorks, J. E., and Braun, S. A.: Investigation of Microphysics
1068 and Precipitation for Atlantic Coast-Threatening Snowstorms (IMPACTS) Collection,
1069 Dataset available online from the NASA Global Hydrometeorology Resource Center
1070 DAAC, Huntsville, Alabama, USA [data set],
1071 <https://doi.org/10.5067/IMPACTS/DATA101>, 2019.
- 1072 McMurdie, L. A., Heymsfield, G. M., Yorks, J. E., Braun, S. A., Skofronick-Jackson, G.,
1073 Rauber, R. M., Yuter, S., Colle, B., McFarquhar, G. M., Poellot, M., Novak, D. R., Lang,
1074 T. J., Kroodsma, R., McLinden, M., Oue, M., Kollias, P., Kumjian, M. R., Greybush, S.
1075 J., Heymsfield, A. J., Finlon, J. A., McDonald, V. L., and Nicholls, S.: Chasing
1076 Snowstorms: The Investigation of Microphysics and Precipitation for Atlantic Coast-
1077 Threatening Snowstorms (IMPACTS) Campaign, *B. Am. Meteorol. Soc.*, 103, E1243–
1078 E1269, <https://doi.org/10.1175/BAMS-D-20-0246.1>, 2022a.
- 1079 McMurdie, L. A., Finlon, J. A., Heymsfield, G. M., and Yorks, J. E.: Investigation of
1080 Microphysics and Precipitation for Atlantic Coast Threatening Snowstorms (Impacts):
1081 The 2022 Deployment, in: *IGARSS 2022 - 2022 IEEE International Geoscience and*
1082 *Remote Sensing Symposium*, Kuala Lumpur, Malaysia, 4461–4464,
1083 <https://doi.org/10.1109/IGARSS46834.2022.9883693>, 2022b.
- 1084 Miller, J. E.: On the Concept of Frontogenesis, *J. Meteorol.*, 5, 169–171,
1085 [https://doi.org/10.1175/1520-0469\(1948\)005<0169:OTCOF>2.0.CO;2](https://doi.org/10.1175/1520-0469(1948)005<0169:OTCOF>2.0.CO;2), 1948.
- 1086 Mitchell, D. L.: Use of Mass- and Area-Dimensional Power Laws for Determining Precipitation
1087 Particle Terminal Velocities, *J. Atmos. Sci.*, 53, 1710–1723,
1088 [https://doi.org/10.1175/1520-0469\(1996\)053<1710:UOMAAD>2.0.CO;2](https://doi.org/10.1175/1520-0469(1996)053<1710:UOMAAD>2.0.CO;2), 1996.
- 1089 Morrison, H., Van Lier-Walqui, M., Fridlind, A. M., Grabowski, W. W., Harrington, J. Y.,
1090 Hoose, C., Korolev, A., Kumjian, M. R., Milbrandt, J. A., Pawlowska, H., Posselt, D. J.,
1091 Prat, O. P., Reimel, K. J., Shima, S., Van Dierenhoven, B., and Xue, L.: Confronting the
1092 Challenge of Modeling Cloud and Precipitation Microphysics, *J. Adv. Model Earth Syst.*,
1093 12, e2019MS001689, <https://doi.org/10.1029/2019MS001689>, 2020.
- 1094 Nelson, J.: Sublimation of Ice Crystals, *J. Atmos. Sci.*, 55, 910–919,
1095 [https://doi.org/10.1175/1520-0469\(1998\)055<0910:SOIC>2.0.CO;2](https://doi.org/10.1175/1520-0469(1998)055<0910:SOIC>2.0.CO;2), 1998.
- 1096 Novak, D. R., Bosart, L. F., Keyser, D., and Waldstreicher, J. S.: An Observational Study of
1097 Cold Season–Banded Precipitation in Northeast U.S. Cyclones, *Weather Forecast.*, 19,
1098 993–1010, <https://doi.org/10.1175/815.1>, 2004.
- 1099 Novak, D. R., Waldstreicher, J. S., Keyser, D., and Bosart, L. F.: A Forecast Strategy for
1100 Anticipating Cold Season Mesoscale Band Formation within Eastern U.S. Cyclones,
1101 *Weather Forecast.*, 21, 3–23, <https://doi.org/10.1175/WAF907.1>, 2006.
- 1102 Novak, D. R., Colle, B. A., and Yuter, S. E.: High-Resolution Observations and Model
1103 Simulations of the Life Cycle of an Intense Mesoscale Snowband over the Northeastern
1104 United States, *M. Weather Rev.*, 136, 1433–1456,
1105 <https://doi.org/10.1175/2007MWR2233.1>, 2008.
- 1106 Petty, G. W. and Huang, W.: Microwave Backscatter and Extinction by Soft Ice Spheres and
1107 Complex Snow Aggregates, *J. Atmos. Sci.*, 67, 769–787,
1108 <https://doi.org/10.1175/2009JAS3146.1>, 2010.
- 1109 Plummer, D. M., McFarquhar, G. M., Rauber, R. M., Jewett, B. F., and Leon, D. C.: Structure
1110 and Statistical Analysis of the Microphysical Properties of Generating Cells in the



- 1111 Comma Head Region of Continental Winter Cyclones, *J. Atmos. Sci.*, 71, 4181–4203,
1112 <https://doi.org/10.1175/JAS-D-14-0100.1>, 2014.
- 1113 Pruppacher, H. R. and Klett, J. D.: *Microphysics Of Clouds And Precipitation*, 2nd rev. and enl.
1114 ed., Kluwer Academic Publishers, Dordrecht; Boston, 954 pp., 1997.
- 1115 Rauber, R. M. and Tokay, A.: An Explanation for the Existence of Supercooled Water at the Top
1116 of Cold Clouds, *J. Atmos. Sci.*, 48, 1005–1023, [https://doi.org/10.1175/1520-0469\(1991\)048<1005:AEFTEO>2.0.CO;2](https://doi.org/10.1175/1520-0469(1991)048<1005:AEFTEO>2.0.CO;2), 1991.
- 1118 Rosenow, A. A., Plummer, D. M., Rauber, R. M., McFarquhar, G. M., Jewett, B. F., and Leon,
1119 D.: Vertical Velocity and Physical Structure of Generating Cells and Convection in the
1120 Comma Head Region of Continental Winter Cyclones, *J. Atmos. Sci.*, 71, 1538–1558,
1121 <https://doi.org/10.1175/JAS-D-13-0249.1>, 2014.
- 1122 Roy, P., Rauber, R. M., and Di Girolamo, L.: A Closer Look at the Evolution of Supercooled
1123 Cloud Droplet Temperature and Lifetime in Different Environmental Conditions with
1124 Implications for Ice Nucleation in the Evaporating Regions of Clouds, *J. Atmos. Sci.*, 80,
1125 2481–2501, <https://doi.org/10.1175/JAS-D-22-0239.1>, 2023.
- 1126 Schnaiter, F. M.: Particle Habit Imaging and Polar Scattering Probe (PHIPS) IMPACTS, Dataset
1127 available online from the NASA Global Hydrometeorology Resource Center DAAC,
1128 Huntsville, Alabama, USA [data set],
1129 <https://doi.org/10.5067/IMPACTS/PHIPS/DATA101>, 2020.
- 1130 Stark, D., Colle, B. A., and Yuter, S. E.: Observed Microphysical Evolution for Two East Coast
1131 Winter Storms and the Associated Snow Bands, *M. Weather Rev.*, 141, 2037–2057,
1132 <https://doi.org/10.1175/MWR-D-12-00276.1>, 2013.
- 1133 Thornhill, K. L.: Turbulent Air Motion Measurement System (TAMMS) IMPACTS, Dataset
1134 available online from the NASA Global Hydrometeorology Resource Center DAAC,
1135 Huntsville, Alabama, USA [data set],
1136 <https://doi.org/10.5067/IMPACTS/TAMMS/DATA101>, 2022.
- 1137 Thornhill, K. L., Anderson, B. E., Barrick, J. D. W., Bagwell, D. R., Friesen, R., and Lenschow,
1138 D. H.: Air Motion Intercomparison Flights during Transport and Chemical Evolution in
1139 the Pacific (TRACE-P)/ACE-ASIA, *J. Geophys. Res.-Atmos.*, 108, 2002JD003108,
1140 <https://doi.org/10.1029/2002JD003108>, 2003.
- 1141 Waldstreicher, J. and Brodzik, S.: NOAA Sounding IMPACTS, Dataset available online from
1142 the NASA Global Hydrometeorology Resource Center DAAC, Huntsville, Alabama,
1143 USA [data set], <https://doi.org/10.5067/IMPACTS/SOUNDING/DATA201>, 2022.
- 1144 Williams, C. R.: How Much Attenuation Extinguishes mm-Wave Vertically Pointing Radar
1145 Return Signals?, *Remote Sens.*, 14, 1305, <https://doi.org/10.3390/rs14061305>, 2022.
- 1146 Yang-Martin, M. and Bennett, R.: P-3 Meteorological and Navigation Data IMPACTS, Dataset
1147 available online from the NASA Global Hydrometeorology Resource Center DAAC,
1148 Huntsville, Alabama, USA [data set], <https://doi.org/10.5067/IMPACTS/P3/DATA101>,
1149 2022.
- 1150 Zaremba, T. J., Rauber, R. M., Heimes, K., Yorks, J. E., Finlon, J. A., Nicholls, S. D., Selmer, P.,
1151 McMurdie, L. A., and McFarquhar, G. M.: Cloud-Top Phase Characterization of
1152 Extratropical Cyclones over the Northeast and Midwest United States: Results from
1153 IMPACTS, *J. Atmos. Sci.*, 81, 341–361, <https://doi.org/10.1175/JAS-D-23-0123.1>, 2024.
- 1154 Zhang, J., Howard, K., Langston, C., Vasiloff, S., Kaney, B., Arthur, A., Van Cooten, S.,
1155 Kelleher, K., Kitzmiller, D., Ding, F., Seo, D.-J., Wells, E., and Dempsey, C.: National
1156 Mosaic and Multi-Sensor QPE (NMQ) System: Description, Results, and Future Plans,

<https://doi.org/10.5194/egusphere-2024-3423>
Preprint. Discussion started: 11 November 2024
© Author(s) 2024. CC BY 4.0 License.



1157 B. Am. Meteorol. Soc., 92, 1321–1338, <https://doi.org/10.1175/2011BAMS-D-11->
1158 00047.1, 2011.